Cell Reports

Article

# *Drosophila* HNF4 acts in distinct tissues to direct a switch between lipid storage and export in the gut

## Graphical abstract

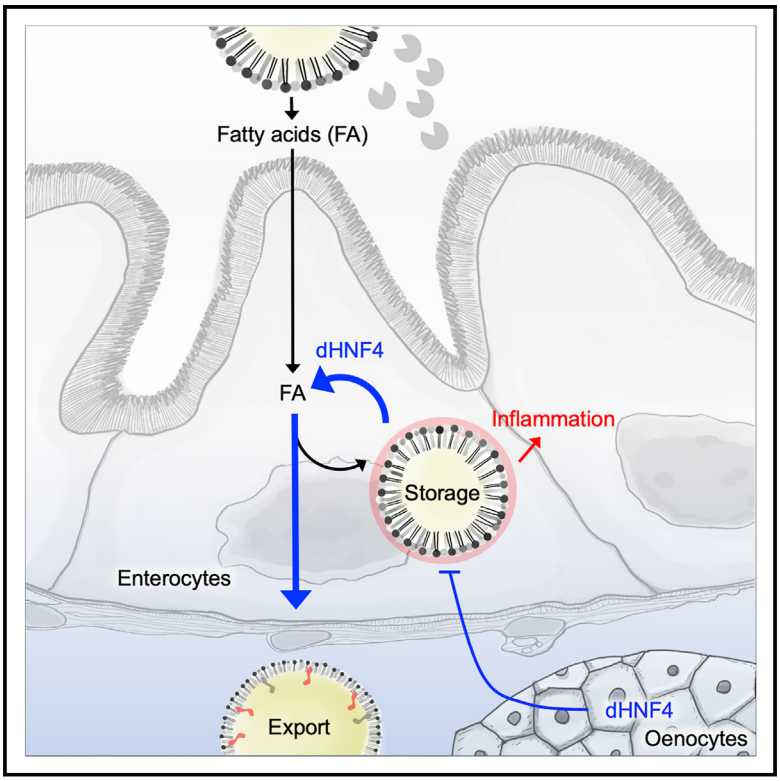


## Highlights

- Specific enterocyte populations absorb dietary lipids in the *Drosophila* intestine
- Enterocyte lipid storage and export are remotely controlled by oenocytes
- *Drosophila* HNF4 acts in both cell types to regulate inter-organ lipid trafficking
- Abnormal lipid storage in the intestine induces local inflammation

## Authors

Maximilian C. Vonolfen, Fenja L. Meyer zu Altenschildesche, Hyuck-Jin Nam, ..., Geanette Lam, Carl S. Thummel, Gilles Storelli

## Correspondence

gstorell@uni-koeln.de

## In brief

Vonolfen et al. show that *Drosophila* hepatocyte nuclear factor 4 acts in enterocytes and oenocytes to coordinate intestinal lipid storage and export. These regulations suppress intestinal steatosis while maintaining body fat levels. They also suppress manifestations of inflammatory bowel diseases, suggesting links between these intestinal disorders and impaired lipid export.

Vonolfen et al., 2024, Cell Reports *43*, 114693
September 24, 2024 
https://doi.org/10.1016/j.celrep.2024.114693

CellPress

Cell Reports

CellPress
OPEN ACCESS

Article

# *Drosophila* HNF4 acts in distinct tissues to direct a switch between lipid storage and export in the gut

Maximilian C. Vonolfen,[1,2] Fenja L. Meyer zu Altenschildesche,[1,2,6] Hyuck-Jin Nam,[3,6] Susanne Brodesser,[4] Akos Gyenis,[4] Jan Buellesbach,[5] Geanette Lam,[3] Carl S. Thummel,[3] and Gilles Storelli[1,2,7,*]

[1]University of Cologne, Faculty of Mathematics and Natural Sciences, Cluster of Excellence Cellular Stress Responses in Aging-associated Diseases (CECAD), Joseph-Stelzmann-Strasse 26, 50931 Cologne, Germany
[2]Institute for Genetics, Faculty of Mathematics and Natural Sciences, University of Cologne, Cologne, Germany
[3]Department of Human Genetics, University of Utah School of Medicine, Salt Lake City, UT 84112-5330, USA
[4]University of Cologne, Faculty of Medicine and University Hospital of Cologne, Cluster of Excellence Cellular Stress Responses in Aging-associated Diseases (CECAD), Joseph-Stelzmann-Strasse 26, 50931 Cologne, Germany
[5]Institute for Evolution & Biodiversity, University of Münster, Hüfferstrasse 1, 48149 Münster, Germany
[6]These authors contributed equally
[7]Lead contact
*Correspondence: gstorell@uni-koeln.de
https://doi.org/10.1016/j.celrep.2024.114693

## SUMMARY

Nutrient digestion, absorption, and export must be coordinated in the gut to meet the nutritional needs of the organism. We used the *Drosophila* intestine to characterize the mechanisms that coordinate the fate of dietary lipids. We identified enterocytes specialized in absorbing and exporting lipids to peripheral organs. Distinct hepatocyte-like cells, called oenocytes, communicate with these enterocytes to adjust intestinal lipid storage and export. A single transcription factor, *Drosophila* hepatocyte nuclear factor 4 (dHNF4), supports this gut-liver axis. In enterocytes, dHNF4 maximizes dietary lipid export by preventing their sequestration in cytoplasmic lipid droplets. In oenocytes, dHNF4 promotes the expression of the insulin antagonist ImpL2 to activate Foxo and suppress lipid retention in enterocytes. Disruption of this switch between lipid storage and export is associated with intestinal inflammation, suggesting a lipidic origin for inflammatory bowel diseases. These studies establish dHNF4 as a central regulator of intestinal metabolism and inter-organ lipid trafficking.

## INTRODUCTION

The digestive system is responsible for some of the most basic functions that support animal life: it digests, absorbs, and exports nutrients to peripheral tissues. These processes must be tightly coordinated to meet the nutritional needs of the organism. How this coordination is achieved remains poorly understood. For example, a nutritious meal triggers the secretion of lipid-rich chylomicrons by enterocytes (ECs) before food actually reaches the small intestine.[1] This phenomenon, known as the "second meal effect," demonstrates that ECs can store dietary fats and selectively retain or export lipids.[1–3] It also suggests that this switch between lipid storage and export is controlled by nutrient sensing and peripheral organs.[1,2] Characterizing the mechanisms that underlie the second meal effect, or, more broadly, that dictate the fate of dietary lipids in the intestine, could have important implications for metabolic health. These discoveries could, for example, benefit the treatment of disorders such as obesity or type 2 diabetes.[2,4,5]

Hepatocyte nuclear factor 4 (HNF4) is a member of the nuclear receptor (NR) superfamily of ligand-regulated transcription factors. It binds fatty acids (FAs) and plays evolutionarily conserved roles in the regulation of lipid metabolism.[6–15] The genome of mammals encodes two HNF4 paralogs, HNF4A and HNF4G, which play redundant roles in the intestine.[12,16,17] The use of *HNF4A/G* double-mutant mice has shown that this NR supports intestinal stem cell renewal and may exert these effects by promoting FA oxidation.[12,16,18] However, *HNF4A/G* double-mutant mice must be rapidly euthanized due to severe intestinal defects, which hinders the discovery of other metabolic roles of HNF4 in the digestive system.[12,16,18] Although HNF4 has undergone duplications during animal evolution, the *Drosophila* genome encodes a single ortholog called *Drosophila* HNF4 (dHNF4).[6,17] This lack of genetic redundancy, combined with the sophisticated genetic tools available in *Drosophila*, provides an ideal context for characterizing the ancestral functions of this NR in the intestine.[11,12,15]

Here, we show that dHNF4 suppresses lipid accumulation (steatosis) in specific sections of the *Drosophila* intestine, revealing a strict regionalization of lipid handling in this organ. We identified ECs that rely on circulating lipoproteins to accumulate lipids, supporting the existence of a basolateral track for triglyceride uptake in the intestine.[1] Another population of ECs absorbs dietary fats and communicates with distant oenocytes to

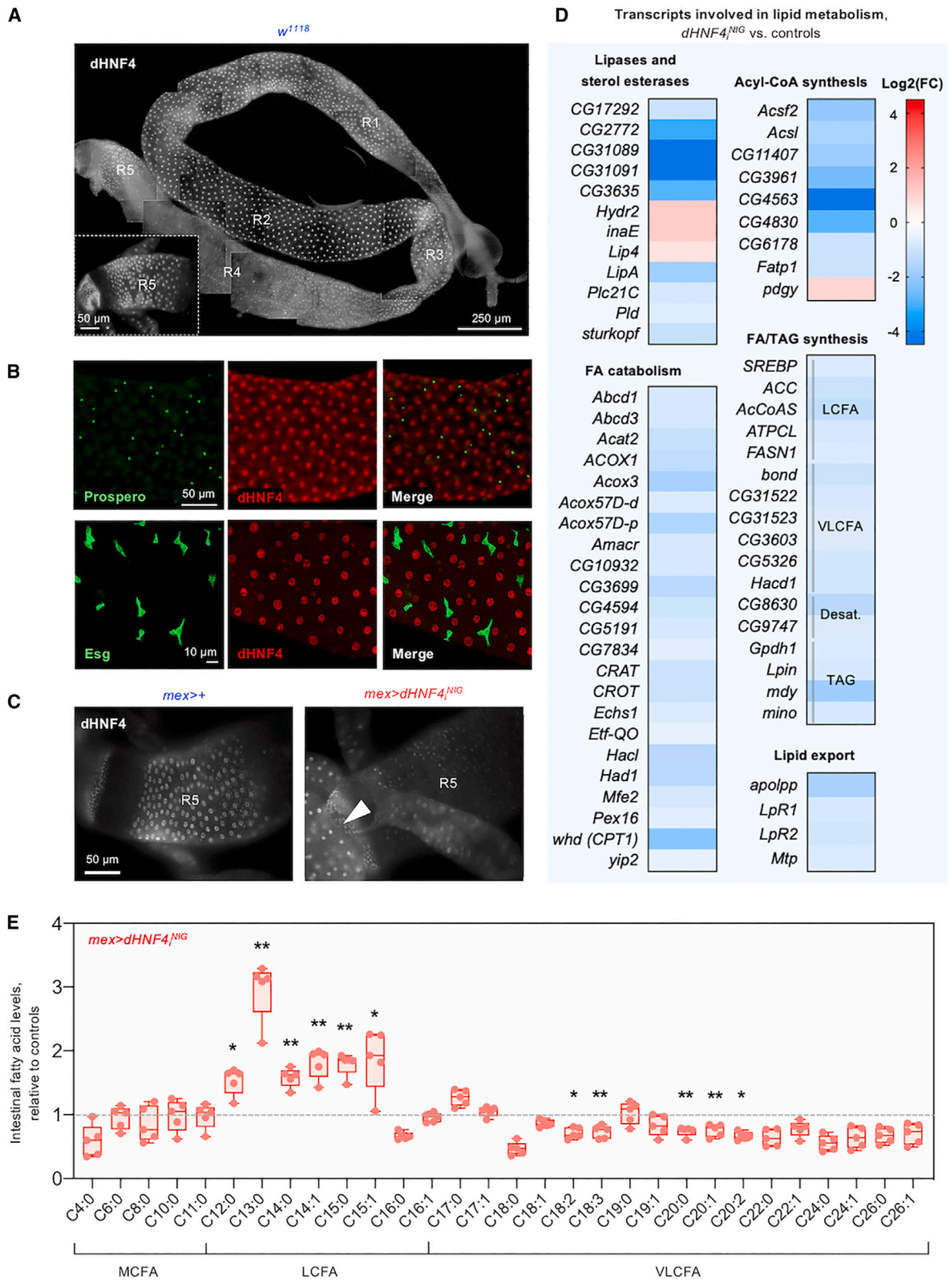


(legend on next page)

regulate intestinal lipid storage and export. dHNF4 plays a central role in this crosstalk. In fat-absorbing ECs, dHNF4 prevents lipid incorporation into cytoplasmic droplets by maintaining the continuous mobilization of these organelles. This directs lipids to the secretory pathway, maximizing their export. In oenocytes, dHNF4 promotes the expression of ImpL2, an antagonist of insulin-like peptides, to activate Foxo in ECs and suppress steatosis in these cells. Finally, abnormal lipid retention in the intestine is associated with hallmark manifestations of inflammatory bowel diseases (IBDs).

Taken together, our work establishes dHNF4 as a central regulator of intestinal lipid metabolism and inter-organ lipid trafficking. It also identifies mechanisms by which peripheral tissues control the decision whether to store or export dietary lipids in ECs and supports the model that defects in these processes can lead to gut inflammatory disorders.

## RESULTS

### dHNF4 is a central regulator of lipid metabolism in the gut

For consistency with previous work (and unless otherwise stated), we performed our studies with adult *Drosophila* males fed a yeast diet without added sugars.[15,19] The *Drosophila* midgut is the main section of the gastrointestinal tract responsible for nutrient digestion and absorption.[20] It is divided in five regions, R1–R5, with specific anatomical features and metabolic functions[21,22] (Figure 1A). Using antibodies directed against dHNF4, we detected high levels of dHNF4 protein throughout the midgut, with the exception of R4, where *dHNF4* expression varies between animals (Figure 1A). dHNF4 is present in polyploid nuclei characteristic of ECs but largely absent from enteroendocrine cells, intestinal stem cells, and enteroblasts (Figure 1B). Since *dHNF4* is predominantly expressed in ECs, we used loss-of-function approaches to investigate its functions in this cell type. We expressed a *UAS-dHNF4 RNAi* transgene under the control of the *mex-GAL4* driver to deplete dHNF4 selectively in ECs and performed mRNA sequencing (mRNA-seq) (Figure 1C; Table S1). Functional enrichment analysis in the list of transcripts that are up-regulated in *dHNF4* RNAi intestines shows an overrepresentation of Gene Ontology terms related to cell division (Figure S1A). A similar analysis of down-regulated transcripts shows an enrichment for terms related to EC function, including digestion, transmembrane transport, and metabolism (Figure S1B). More particularly, numerous transcripts involved in lipid digestion, lipid transport, lipolysis, and FA catabolism and synthesis are reduced when *dHNF4* is suppressed in this cell type (Figures 1D and S1B–S1E). We confirmed these observations with two alternative *dHNF4* RNAi transgenes and adult-specific deletion of the *dHNF4* locus, thanks to a conditional *dHNF4* allele that we have generated (Figures S1F, S1G, and S2A–S2D). We next sought to determine whether these transcriptional changes were associated with altered FA levels. Consistent with suppressed lipolysis and β-oxidation, the levels of long-chain FAs (LCFAs) are significantly increased in midguts lacking *dHNF4* in ECs (Figure 1E). In contrast, very long-chain FAs (VLCFAs) are depleted, in agreement with reductions in transcripts involved in the synthesis of this class of lipids (Figure 1E).

### dHNF4 suppresses steatosis in specific populations of ECs

We complemented these lipidomic analyses by quantifying cytoplasmic lipid droplets (LDs) in midguts with Oil red O stains. While control intestines contain sparse and small LDs mostly located in R4, the suppression of *dHNF4* in ECs is associated with a marked accumulation of neutral lipids in R3 and R5 and, to a lesser extent, in R2 (Figure 2A). We made similar observations in R3 and R5 of animals with adult-specific deletion of the *dHNF4* locus and with the *dHNF4* mutant alleles that were previously published (Figures 2B and S3A).[11,15,19] Therefore, *dHNF4* suppresses the storage of LCFAs in cytoplasmic LDs in specific compartments of the midgut (Figures 2A and 1E). We also observed differences in the pattern of LD accumulation between R3 and R5 in *dHNF4* RNAi intestines. While R5 contains numerous small- and medium-sized LDs, R3 is filled with few but massive LDs (Figure 2C). A similar pattern was seen in R3 of animals with adult-specific deletion of the *dHNF4* locus (Figure S3B). R3 is the only region of the midgut that contains two markedly different populations of ECs: copper cells and interstitial cells (ICs), both of which express *dHNF4* (Figures 2D and S3C). The copper cells are analogous to gastric parietal cells, and their acidic secretions play microbiocidal roles.[23–26] ICs are less well characterized but were recently shown to regulate food intake.[27] Transmission electron microscopy demonstrates that steatosis in R3 upon pan-EC *dHNF4* silencing is restricted to ICs (Figure 2D). We therefore targeted ICs more specifically

**Figure 1. dHNF4 acts in ECs to regulate intestinal lipid metabolism**

(A and B) Antibodies directed against dHNF4 were used to determine its pattern of expression in control intestines.

(A) The inset shows a higher magnification view of R5, which displays high *dHNF4* expression in enterocytes (ECs).

(B) Anti-dHNF4 antibody stains in guts counterstained with anti-Prospero antibodies to label enteroendocrine cells (top) and guts expressing the transgenic reporter *Esg>GFP* labeling intestinal stem cells and enteroblasts (bottom).

(C) Antibody stains were used to determine the effect of *dHNF4 RNAi*$^{NIG}$ on dHNF4 protein levels in ECs (*mex>dHNF4*$_i^{NIG}$). The white arrowhead indicates a piece of visceral fat where *dHNF4* expression is not affected. The images represent R5 of the adult midgut.

(D) mRNA-seq was performed to detect genome-wide differences in transcript levels between control intestines and intestines lacking *dHNF4* function in ECs (*mex>dHNF4*$_i^{NIG}$). Heatmaps show the levels of transcripts involved in lipid metabolism in *mex>dHNF4*$_i^{NIG}$ intestines. Log2(FC), log2 fold change in levels when compared to controls. Only transcripts with significantly altered levels are shown. $n = 5$ biological replicates.

(E) Total fatty acid (FA) levels were scored by mass spectrometry in *mex>dHNF4*$_i^{NIG}$ intestines. FA levels are shown as relative to control levels (dotted line). "Cx:y" indicates the fatty acyl chains, where x is the number of carbon atoms and y the number of double bonds. MCFA, LCFA, and VLCFA, medium-, long-, and very-long-chain fatty acids. Data are from one experiment. Dots: biological replicates, $n = 5$, line: median, whiskers: minimum and maximum values. Asterisks indicate statistically significant differences with controls. $0.001 < **p < 0.01$ and $0.01 < *p < 0.05$ (Mann-Whitney test).

See also Figure S1 and Table S1.

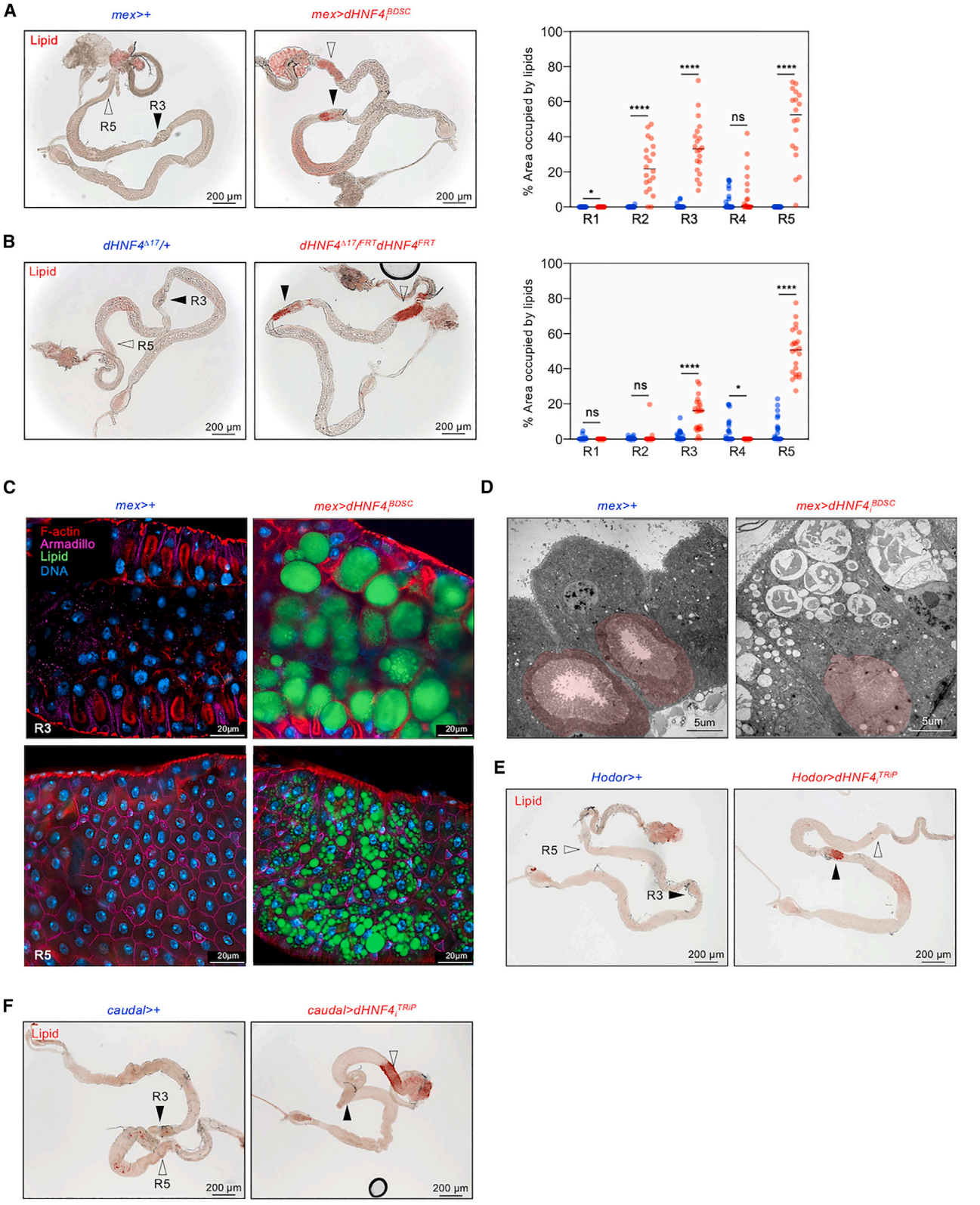


*(legend on next page)*

by expressing different *UAS-dHNF4 RNAi* transgenes with *Hodor-GAL4*, a driver that is active in ICs but not copper cells (Figure S3D).[27] These manipulations induce steatosis in R3, supporting that *dHNF4* acts in ICs to suppress LD formation in this region (Figures 2E and S3E). In parallel, we expressed *dHNF4 RNAi* specifically in R5 ECs by using the *caudal-GAL4* driver (Figure S3F). This manipulation induces lipid accumulation in the distalmost part of the midgut (Figure 2F). These observations demonstrate that dHNF4 acts in a cell-autonomous manner to suppress lipid accumulation in ICs and R5 ECs.

## dHNF4 promotes lipid efflux from ICs and R5 ECs

Dietary fat is broken down by digestive lipases in the gut lumen to generate free FAs. Free FAs are then absorbed by ECs, where they are stored in cytoplasmic LDs or loaded onto lipoproteins for export to peripheral tissues (Figure 3A). R3 and R5 display high levels of transcripts encoding digestive and cytoplasmic lipases and become steatotic upon *dHNF4* silencing (Figures S4A, 2E, and 2F). These regions could therefore digest, absorb, and export dietary lipids, and dHNF4 could support these functions. While mammalian ECs are autonomous in the synthesis of chylomicrons,[3] *Drosophila* ECs rely on lipoproteins that are produced by the adipose tissue.[28–31] The synthesis of lipoproteins (also called ''lipophorins'') requires the microsomal triacylglycerol transfer protein (Mtp), the apolipoprotein lipid transfer particle (LTP), the apolipophorin Lpp, and the exchangeable apolipoprotein Nplp2.[28–31] Lipoproteins are secreted into the circulation and reach the gut, where they are further loaded with lipids (Figure 3A). Blocking lipophorin synthesis by silencing *Nplp2*, *Lpp*, or *Mtp* in the whole organism induces LD accumulation in R3 and R5, demonstrating that these midgut regions export lipids (Figures 3B and 3C). Similar effects are seen when *Lpp*, *LTP*, or *Mtp* are suppressed in the fat body (Figure S4B). We then checked if dietary fats support LD formation in the midgut when lipophorins or *dHNF4* are suppressed. For this, we prepared lipid-free diets with either water-soluble yeast extract or yeast that was subjected to lipid extraction. Both lipid-free diets reduce midgut steatosis upon *Nplp2* or *dHNF4* suppression, confirming that dietary fats promote LD formation under these conditions (Figures 3D–3F, S4C, and S4D). Since animals lacking *dHNF4* in ECs do not eat more than their control siblings, midgut steatosis may result from impaired lipid export (Figure S4E). Consistent with this hypothesis, major triglyceride species accumulate in the midgut but are depleted in whole animals upon *dHNF4* suppression in ECs (Figures S4F and 3G). In particular, triglycerides are depleted in the thorax, which contains adipose tissue and flight muscles (Figures S4G and S4H). We found no difference in circulating lipid levels when *Nplp2* or *dHNF4* was suppressed in the whole animal or ECs, respectively (Figure S4I). However, these analyses could be complicated by the circadian rhythmicity and inter-individual variability of feeding in males (Figure S4E). Taken together, these data show that dHNF4 suppresses dietary lipid retention in ECs to support lipid storage in peripheral tissues.

## dHNF4 controls a switch between lipid storage and export in ECs

ECs express the lipophorin receptors LpR1 and LpR2, which mediate lipophorin uptake from the circulation (Figures S4J and 3A).[28–32] Reduced *LpR1* and *LpR2* transcript levels may therefore contribute to lipid accumulation upon loss of *dHNF4* (Figures 1D and S2D). Silencing *LpR1* or *LpR2* in the ECs of otherwise wild-type animals does not induce gut steatosis (Figure S4K). However, each receptor could compensate for the loss of the other. Therefore, we blocked receptor-mediated lipophorin uptake by suppressing endocytosis with *Rab5* RNAi. This induces lipid retention in R3 and R5, consistent with the observations made with inhibition of lipophorin synthesis (Figures S4L and 3B). Therefore, dHNF4 may suppress lipid accumulation by promoting *LpR1* and *LpR2* expression and lipophorin uptake. dHNF4 could also directly suppress the storage of free FAs in cytoplasmic LDs. This would limit steatosis but also maximize FA incorporation into lipoproteins. Consistent with this possibility, dHNF4 directs the expression of cellular lipases and promotes intestinal lipolytic activity (Figures 3H and 1D). We set out to determine if some of the predicted lipases regulated by dHNF4 control midgut lipid levels (Figures S4M–S4O). Lipase A (LipA; also known as magro[33]) is a lysosomal sterol esterase that is highly expressed in R3 (Figure S4A). Its expression is reduced upon *dHNF4* RNAi, and *LipA* suppression in otherwise wild-type guts leads to significant lipid accumulation in R3 (Figures S4M and 1D). We made similar observations upon pan-EC silencing of *CG2772*, *CG3635*, *Plc21c*, and *Pld* (Figures S4N and 1D). In contrast, suppression of *CG31089* and *CG31091* is associated with significant lipid accumulation in both R3 and R5 (Figures S4O and 1D). Therefore, dHNF4 is likely to act through several region-specific lipases to suppress LD formation in R3 and R5. We next sought to determine the

**Figure 2. dHNF4 is required in specific EC populations to suppress steatosis**

(A and B) Oil red O was used to stain neutral lipids in (A) intestines in which *dHNF4* is suppressed in ECs (*mex>dHNF4*$_i^{BDSC}$) and (B) intestines of animals with adult-specific *dHNF4* deletion (*dHNF4*$^{\Delta 17/FRT}$*dHNF4*$^{FRT}$). Left: representative pictures. Right: percentage of area occupied by lipids in the different regions of the midgut.

(C) BODIPY (green) was used to stain neutral lipids in control intestines and intestines in which *dHNF4* is suppressed in ECs (*mex>dHNF4*$_i^{BDSC}$). Anti-Armadillo antibodies (magenta), Alexa Fluor 555 Phalloidin (red), and DAPI (blue) label intercellular junctions, F-actin, and DNA, respectively. Tissues were imaged using confocal microscopy. Top: representative transverse views of R3. Bottom: representative pictures of R5; the focal plane is close to the apical surface of ECs.

(D) Electron microscopy was used to obtain transverse views of R3 in control and *mex>dHNF4*$_i^{BDSC}$ intestines. Copper cells are artificially colored in red to distinguish them from interstitial cells.

(E and F) Oil red O was used to stain neutral lipids in intestines with *dHNF4* silencing in (E) interstitial cells or (F) R5 ECs (*Hodor>dHNF4*$_i^{TRiP}$ and *caudal>dHNF4*$_i^{TRiP}$, respectively).

(A, B, E, and F) R3 and R5 are indicated by closed and open arrowheads, respectively. (A and B) Data are from three independent experiments. Dots: biological replicates, $23 > n > 16$, line: median, $^{****}p < 0.0001$; $0.01 < {}^{*}p < 0.05$; ns, no statistically significant difference (Mann-Whitney test).

See also Figures S2 and S3.

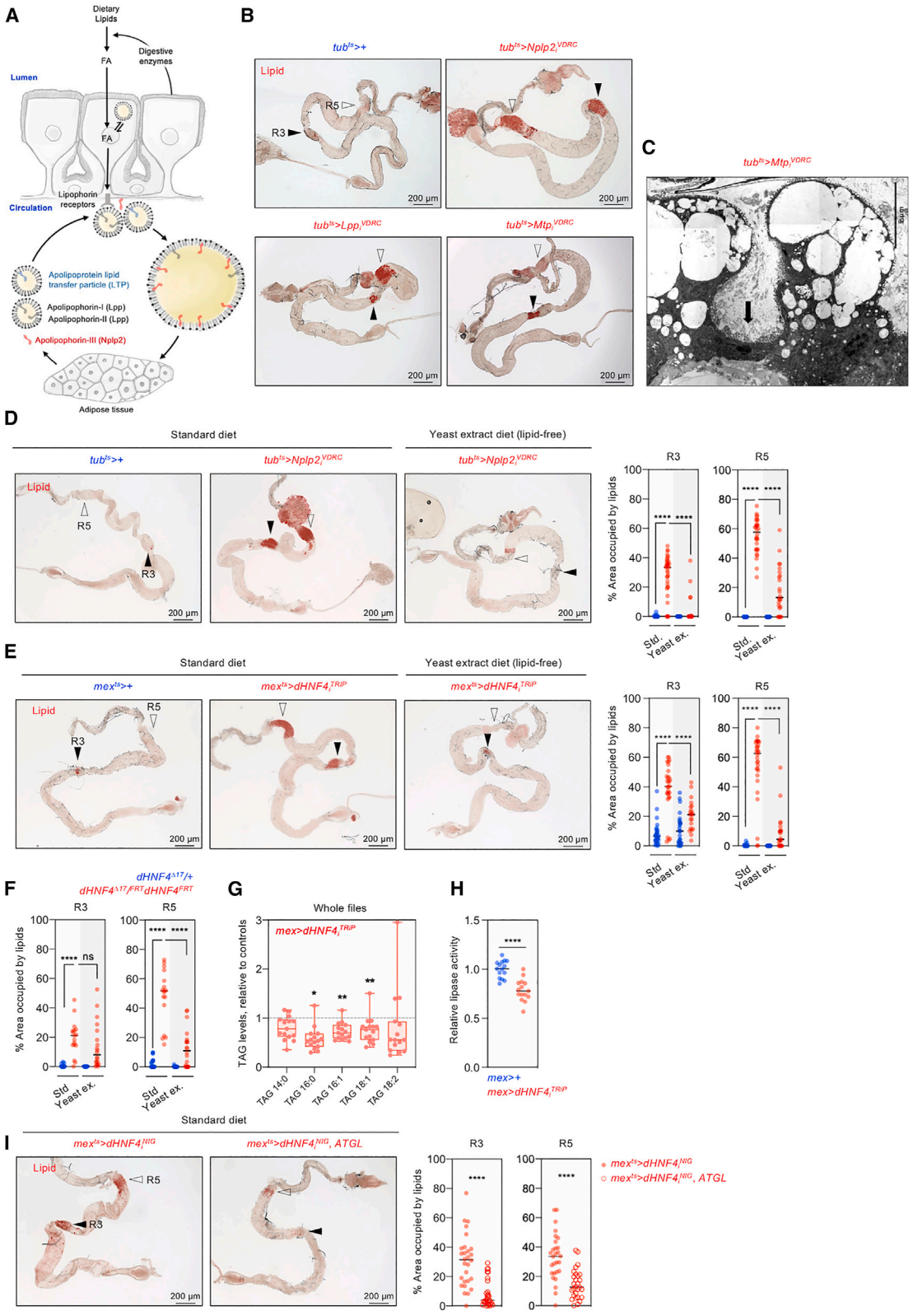


(legend on next page)

contribution of reduced lipolysis to steatosis in *dHNF4* RNAi midguts. To do this, we genetically enhanced LD mobilization by expressing the adipose triglyceride lipase in ECs (ATGL is also known as brummer) (Figure 3I). This significantly reduces intestinal lipid levels, demonstrating that steatosis upon loss of *dHNF4* is largely due to reduced LD mobilization rather than impaired lipophorin uptake.

## dHNF4 suppresses sugar-induced lipid accumulation in R2 ECs

A lipid-free diet does not fully suppress R3 and R5 steatosis upon *Nplp2* or *dHNF4* suppression, suggesting that R3 and R5 ECs also use dietary carbohydrates to perform *de novo* lipogenesis (Figures 3D–3F, S4C, and S4D). To test this possibility, we supplemented the diet with sucrose and scored the formation of ectopic LDs in control intestines. Sugar feeding does not induce LD formation in R3 and R5 but promotes steatosis in R2 and R4 in control guts (Figure 4A). This suggests that R2 and R4 preferentially use carbohydrates to produce lipids and could export their products to the periphery. If this is the case, then blocking inter-organ lipid transport should exacerbate R2 and R4 steatosis following sugar feeding. However, the suppression of *Nplp2* does not affect lipid levels in R4 and even suppresses steatosis in R2 in sugar-fed animals (Figure 4B). Therefore, R2 and R4 do not export lipids, and R2 may actually depend on circulating lipoproteins to accumulate LDs. In contrast to the effects of *Nplp2* RNAi, suppression of *dHNF4* exacerbates R2 steatosis under sugar feeding (Figure 4C). dHNF4 could therefore limit steatosis in R2 by promoting LD mobilization rather than lipid export, as previously shown in R3 and R5 (Figure 3I). We next sought to determine if *dHNF4* acts directly in R2 ECs to limit steatosis in these cells. We used *Mal-A7-GAL4* to express *dHNF4* RNAi specifically in R2 and R4 ECs (Figure S3G). This manipulation induces mild steatosis in R4 independently of the presence of sugar in the diet (Figure 4D, right graph). However, it induces mild steatosis in R2 of animals fed a standard diet, which is dramatically exacerbated following sugar feeding (Figure 4D, left graph). We made similar observations in R2 when we expressed *dHNF4* RNAi with *Hodor-GAL4*, which is active in the anterior half of this region (Figures 4E and S3D). Therefore, R2 ECs store lipids in response to sugar feeding, and dHNF4 limits sugar-dependent LD formation in these cells. In contrast to what was seen in R2, dietary sugars reduce steatosis in ICs and R5 ECs when *dHNF4* is silenced in these cells (Figures 4F and 4G). Given that R3 and R5 are specialized in lipid absorption, these effects could be explained by the well-known repression of digestive lipases by dietary sugars (Figure 4H).[34,35] Therefore, dietary lipids and sugars promote LD formation in distinct EC populations, and dHNF4 acts in these cells to limit steatosis.

## dHNF4 acts in oenocytes to control intestinal lipid storage

Systemic and EC-specific loss of *dHNF4* have different effects on intestinal lipid distribution (Figures 2A and 2B). dHNF4 could therefore also act in peripheral tissues to control intestinal lipid levels. To test this possibility, we suppressed *dHNF4* in major metabolic organs and scored lipid accumulation in the intestine of animals fed a standard diet without added sugars. Adipose tissue (also known as fat body in *Drosophila*) is located in the thorax and along the dorsal side of the abdomen, where it contacts the oenocytes (Figure S5A). Oenocytes are often referred to as "hepatocyte-like cells" because of their role in the metabolic response to starvation.[15,36,37] Silencing *dHNF4* in the adipose tissue does not visibly affect intestinal lipid levels (Figure S5B). In contrast, silencing *dHNF4* in oenocytes with different RNAi transgenes induces intestinal steatosis (Figures 5A and S5C). Since this manipulation does not increase food intake, midgut steatosis could result from impaired inter-organ lipid trafficking (Figure S5D). To determine if oenocytes participate in inter-organ lipid trafficking, we silenced several genes involved in lipophorin synthesis in these cells. Silencing *Nplp2* in oenocytes induces lipid retention in the midgut, demonstrating that they produce

**Figure 3. dHNF4 controls a switch between lipid storage and export in interstitial cells and R5 ECs**

(A) Simplified representation of intestinal lipid absorption and inter-organ lipid transport in *Drosophila*. See main text for details.

(B) Oil red O was used to stain neutral lipids in the intestine of animals with systemic suppression of *Nplp2*, *Lpp*, and *Mtp*.

(C) Electron microscopy was used to obtain transverse views of R3 under systemic suppression of *Mtp*. The arrow indicates a copper cell between two interstitial cells filled with lipid droplets (LDs).

(D–F) Oil red O was used to quantify intestinal lipids in animals fed a standard diet or a lipid-free diet prepared with yeast extract and under (D) systemic suppression of *Nplp2*, (E) EC suppression of *dHNF4*, and (F) adult-specific *dHNF4* deletion.

(G) Total triacylglycerol (TAG) levels were determined by mass spectrometry in control animals and animals with pan-EC *dHNF4* silencing (*mex>dHNF4*$_i^{TRiP}$) fed a standard diet. For clarity, only the most abundant TAG species are shown. "TAG x:y" indicates a TAG that contains a fatty acyl chain with x carbon atoms and y double bonds (without further distinction of the two other fatty acyl chains). TAG levels were normalized to the total amount of protein in fly homogenates and are shown as relative to control levels (dotted line). Asterisks indicate statistically significant differences with control levels.

(H) TAG lipase activity was scored in the intestines of *mex>dHNF4*$_i^{TRiP}$ adult males fed a standard diet. Lipase activity was normalized to the amount of protein in tissue homogenates.

(I) Oil red O was used to stain neutral lipids in intestines with *dHNF4* silencing in ECs with or without ectopic *ATGL* expression in these cells.

(B–D) The *tub-GAL4, tub-GAL80*$^{ts}$ ("*tub*$^{ts}$>") transgenes were used for ubiquitous expression RNAi after the onset of adulthood. (E and I) The *mex-GAL4, tub-GAL80*$^{ts}$ ("*mex*$^{ts}$>") transgenes were used for pan-EC *dHNF4* RNAi expression after the onset of adulthood. (D–F) Animals were fed a standard diet during development and switched to a lipid-free diet after the onset of adulthood. (B–E and I) Animals were kept at room temperature during development and transferred to 29°C after the onset of adulthood to induce transgene expression. (B, D, E, and I) R3 and R5 are indicated by closed and open arrowheads, respectively. (D–F and I) The percentage of area occupied by lipids in midgut regions under the different conditions is represented. (D–F, H, and I) Data are from three independent experiments. Dots: biological replicates, $34 > n > 21$, line: median. (G) Data are from three independent experiments. Dots: biological replicates, $n = 15$, line: median, whiskers: minimum and maximum values. (D–I) ****$p < 0.0001$; $0.001 <$ **$p < 0.01$ and $0.01 <$ *$p < 0.05$; ns, no statistically significant difference (Mann-Whitney test).

See also Figure S4.

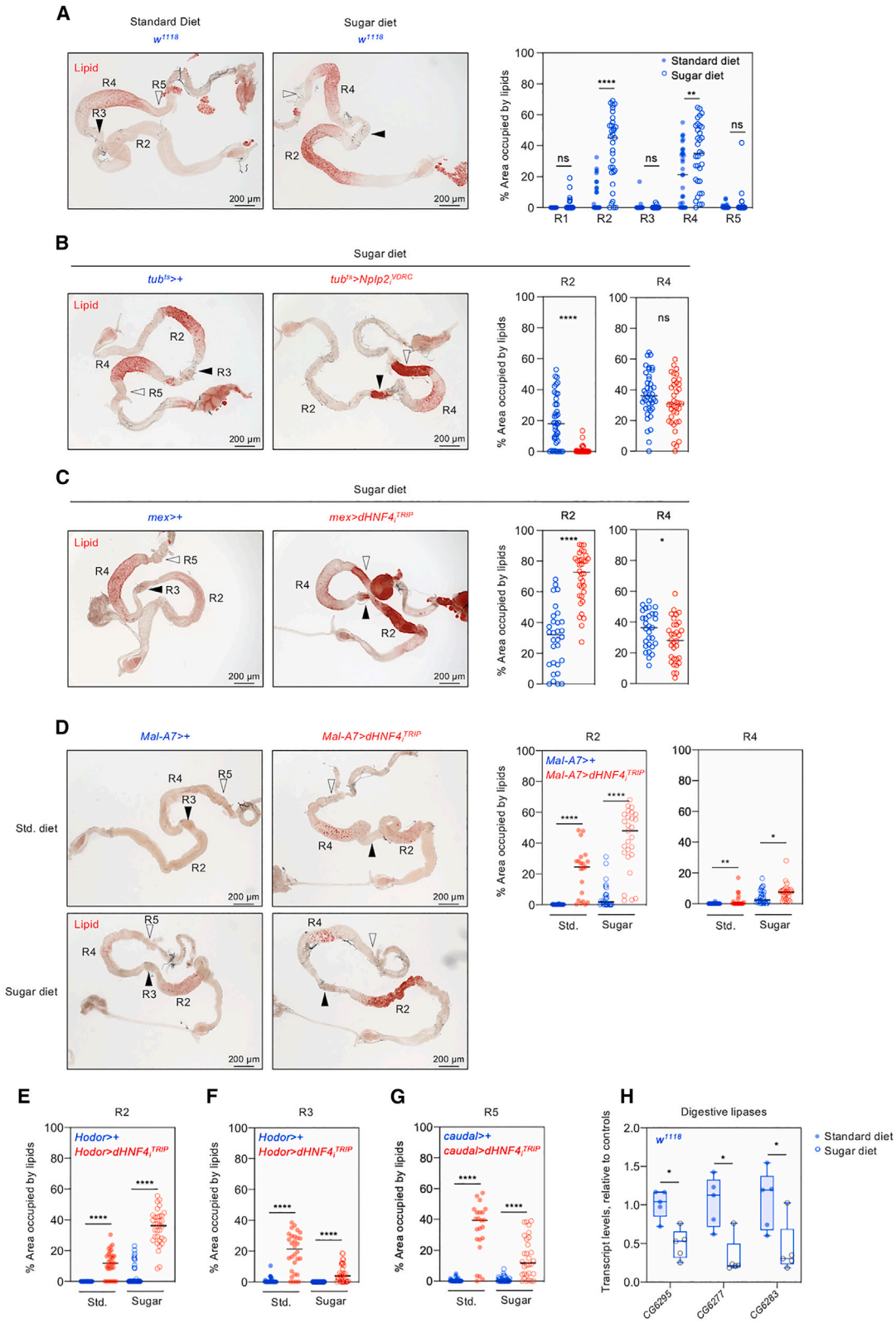


*(legend on next page)*

exchangeable apolipoprotein to facilitate intestinal lipid export (Figure S5E). Since silencing *dHNF4* and *Nplp2* in oenocytes has similar effects on midgut lipid levels, dHNF4 could promote *Nplp2* expression in these cells. However, we observed the opposite, with increased *Nplp2* expression following *dHNF4* RNAi in oenocytes (Figure S5F). Therefore, dHNF4 acts through mechanisms other than the production of Nplp2 in oenocytes to control midgut lipid levels. Oenocytes express high levels of the secreted factor ImpL2, and the *ImpL2* transcript is reduced when *dHNF4* is silenced in oenocytes (Figures S5G and 5B).[38] ImpL2 is a functional analog of the insulin growth factor (IGF)-binding protein 7; it suppresses insulin signaling by sequestering circulating insulin-like peptides.[39,40] Since *ImpL2* expression is reduced following *dHNF4* RNAi in oenocytes, peripheral insulin signaling could be increased under this condition. Accordingly, Foxo is excluded from EC nuclei when *dHNF4* is silenced in oenocytes, and several Foxo transcriptional targets are reduced in fat bodies and oenocytes (Figures 5C and S5H). Consistent with the well-established roles of Foxo in promoting lipolysis, reducing Foxo signaling in ECs leads to significant lipid accumulation in R3 (Figure 5D).[41] Taken together, these observations support a model in which dHNF4 promotes *ImpL2* expression in oenocytes to activate Foxo signaling in ECs, which in turn limits intestinal steatosis. This crosstalk suggests that ECs and oenocytes cooperate in the metabolism of lipids. Oenocytes convert lipids into cuticular hydrocarbons, which act as pheromones and suppress water loss by transpiration.[15,36,37] The blend of cuticular hydrocarbons is markedly altered when *dHNF4* is suppressed in ECs or *Nplp2* is suppressed in the whole organism (Figures 5E and S5I; Table S2). Therefore, gut-derived lipids influence cuticular hydrocarbon production in oenocytes. These observations demonstrate the existence of a gut-liver axis in *Drosophila*, in which dHNF4 plays a central role.

### dHNF4 suppresses intestinal inflammation

In addition to broad defects in lipid metabolism, our transcriptomic analysis has shown an overrepresentation of transcripts involved in cell division in *dHNF4* RNAi intestines (Figure S1A). Consistent with this signature, we detected an increase in intestinal stem cell proliferation when *dHNF4* is suppressed in ECs (Figure 6A). This suggests an activation of regenerative mechanisms in response to tissue stress. Interestingly, variants in *HNF4A* have been associated with IBDs in several patient cohorts.[44–46] In parallel, JNK, JAK/STAT, and Rel/nuclear factor κB (NF-κB) pathways are activated in *dHNF4* mutant flies, but the localization of these responses has not been determined.[19] The suppression of *dHNF4* in ECs with different RNAi transgenes is associated with increased midgut expression of *jun* and its target *puc*, suggesting that JNK is activated under these conditions (Figures 6B and 6C).[47] The expression of *upd2* and *upd3*, two targets of the JNK pathway, is also increased (Figures 6B and 6C). The cytokines upd2 and upd3 activate STAT signaling.[48] Consistent with their increased expression, the level of *Socs36E*, a well-established target of *Drosophila* STAT,[48,49] is also increased (Figures 6B and 6C). However, Rel/NF-κB-related transcripts remain largely unchanged (Figures 6B and 6C). Since the loss of *dHNF4* is associated with intestinal inflammation, this condition could recapitulate other hallmarks of IBDs. Accordingly, we observed an increased sensitivity to experimental colitis, recapitulating previous observations made in *HNF4A* mutant mice[50,51] (Figures S6A–S6C). We then sought to localize JNK activation in the midgut by using the *puc-lacZ* transgenic reporter. JNK is significantly induced in R3 and R5 upon pan-EC *dHNF4* silencing (Figure 6D). Given that dHNF4 suppresses steatosis and stress signaling in these regions, these functions may be physiologically linked. Consistent with this hypothesis, a lipid-free diet suppresses both steatosis and JNK signaling in R5 upon pan-EC *dHNF4* silencing (Figures 6D, 3E, 3F, and S4D). To determine if steatosis is responsible for inducing JNK signaling, we fed control animals a high-fat diet. This treatment induces both steatosis and JNK signaling in R5 (Figures S6D and 6E). Taken together, these observations support the model that dHNF4 suppresses intestinal inflammation by limiting lipid retention in ECs.

## DISCUSSION

### dHNF4 acts in ECs to funnel dietary lipids toward the secretory pathway

Lipids are hydrophobic molecules, posing challenges to their trafficking between organs. To overcome these limitations, ECs package them into water-miscible chylomicrons (or lipoproteins in insects) prior to their secretion into circulation.[1–3,28] ECs can also sequester dietary fats in cytosolic LDs.[1,2] The decision to direct lipids to intracellular storage or the secretory pathway may have a dramatic impact on nutrition and metabolic health, but the mechanisms controlling this switch remain largely unknown.[1–3] We show that dHNF4 funnels FAs to the secretory pathway by suppressing their incorporation into cytoplasmic LDs (Figure 3). The central role of dHNF4 in intestinal lipid

**Figure 4. dHNF4 suppresses sugar-induced lipid accumulation in R2 ECs**

(A) Oil red O was used to stain neutral lipids in the intestine of control animals fed a standard (sugar-free) diet or a diet supplemented with sucrose (sugar diet).

(B) Oil red O was used to stain neutral lipids in the intestine of animals fed a sugar diet following ubiquitous *Nplp2* silencing. The *tub-GAL4, tub-GAL80$^{ts}$* ("*tub$^{ts}$*>") transgenes were used for ubiquitous *Nplp2* RNAi expression after the onset of adulthood.

(C–G) Oil red O was used to stain neutral lipids in the intestine of animals fed standard or sugar diets and under *dHNF4* suppression in (C) all ECs, (D) R2 and R4 ECs (*Mal-A7> dHNF4$_i^{TRiP}$*), (E and F) R2 ECs and interstitial cells (*Hodor> dHNF4$_i^{TRiP}$*), and (G) R5 ECs (*caudal> dHNF4$_i^{TRiP}$*).

(A–D) R3 and R5 are indicated by closed and open arrowheads, respectively. R2 and R4 are also labeled for clarity. (A–G) The percentage of area occupied by lipids in midgut regions under the different conditions is represented.

(H) Representative transcripts encoding digestive lipases were scored by RT-qPCR in animals fed standard or sugar diets.

(A–H) Animals were fed a standard diet during development and switched to a sugar diet after the onset of adulthood. (A–G) Data are from three to four independent experiments. Dots: biological replicates, $41 > n > 21$, line: median. (H) Data are from one representative experiment. Dots: biological replicates, $n = 5$, line: median, whiskers: minimum and maximum values. (A–H) $^{****}p < 0.0001$; $0.001 < {}^{**}p < 0.01$ and $0.01 < {}^{*}p < 0.05$; ns, no statistically significant difference (Mann-Whitney test).

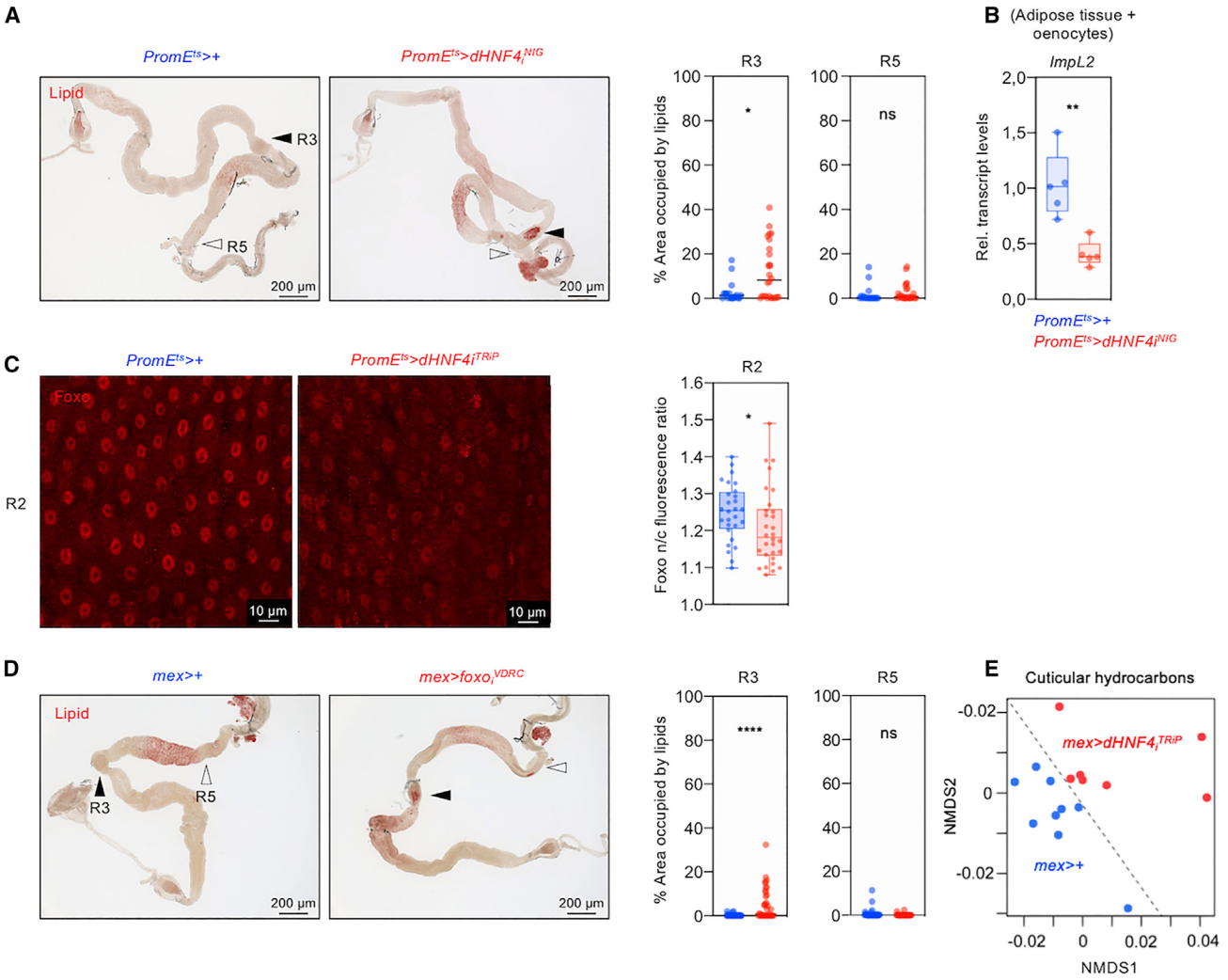


**Figure 5. dHNF4 acts in oenocytes to control intestinal lipid storage**

(A and D) Oil red O was used to stain neutral lipids in the intestine of animals with (A) *dHNF4* silencing in oenocytes or (D) *foxo* silencing in ECs. Left: representative pictures. R3 and R5 are indicated by closed and open arrowheads, respectively. Right: percentage of area occupied by lipids in R3 and R5 under the different conditions.

(B) RT-qPCR analysis of *ImpL2* transcript in abdominal cDNA isolated from controls and animals with adult-specific suppression of *dHNF4* in oenocytes.

(C) Anti-Foxo antibody stains[42] were used to score its nuclear-to-cytoplasmic (n/c) ratio in R2 in animals with adult-specific suppression of *dHNF4* in oenocytes. n/c Foxo ratios were quantified in R2 rather than R3 due to technical limitations described in the STAR Methods. Left: representative confocal fluorescence microscopy images. Right: n/c fluorescence ratios calculated from wide-field fluorescence microscopy images.

(A–C) The *PromE-GAL4, tub-GAL80$^{ts}$* ("*PromE$^{ts}$*>") transgenes were used to drive RNAi expression in oenocytes after the onset of adulthood.

(E) Non-metric multidimensional scaling (NMDS) plot representing cuticular hydrocarbon variation between control animals and animals with *dHNF4* suppression in ECs. An obtained stress value <0.06 indicates reliable ordination with no risk of false inferences.[43] Data are from one experiment. Dots: biological replicates, $n = 9$ (controls) and 7 (*dHNF4* RNAi).

(A and D) Data are from three to four independent experiments. Dots: biological replicates, $39 > n > 17$, line: median. (B and C) Data are from (B) one or (C) three experiments. Dots: biological replicates, (B) $n = 5$, (C) $30 > n > 28$. Line: median, whiskers: minimum and maximum values. (B–D) ****$p < 0.0001$, $0.001 < **p < 0.01$, and $0.01 < *p < 0.05$; ns, no statistically significant difference (Mann-Whitney test).

See also Figure S5 and Table S2.

handling is illustrated by the manifestations of its loss in ECs: intestinal steatosis reaches levels that are similar to those seen upon suppression of inter-organ lipid transport (Figures 3D and 3E). HNF4 is one of the first NRs that appeared during animal evolution, and several of its metabolic functions are conserved between invertebrates and vertebrates.[11,12,15] Our studies may thus provide important insights into the evolutionarily conserved mechanisms that license FAs for intracellular storage or the secretory pathway in ECs but also in other cell types exporting lipids, such as hepatocytes.[11,12,15] Finally, HNF4 is closely associated with gut health and disease but also a druggable target: several synthetic agonists and antagonists have recently been

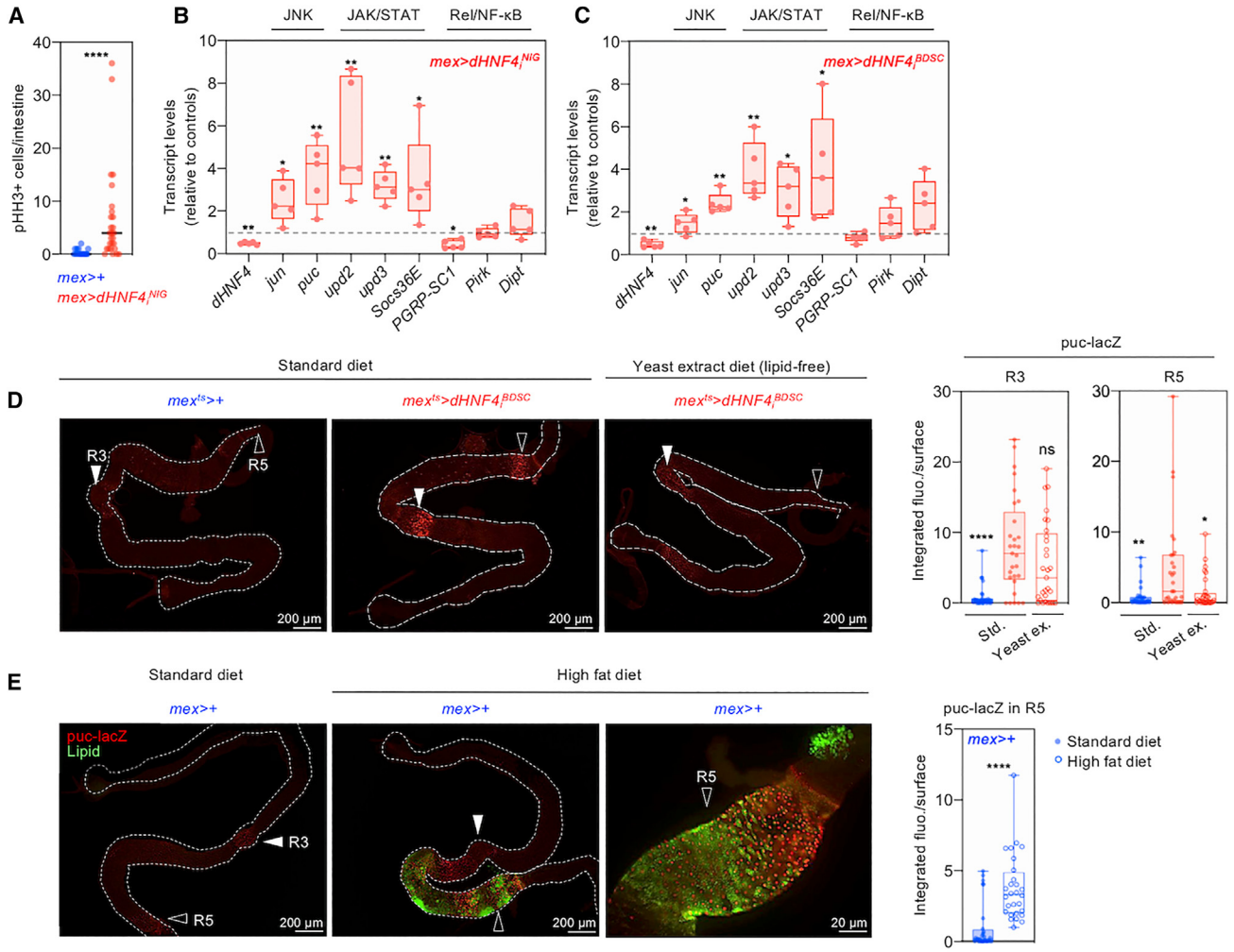


**Figure 6. dHNF4 suppresses intestinal inflammation**

(A) Antibodies directed against phospho-histone H3 (pHH3) were used to score intestinal stem cell mitoses in control and *mex>dHNF4*$_i^{NIG}$ intestines.

(B and C) RT-qPCR analysis of transcripts encoding components of JNK, JAK/STAT, and Rel/NF-κB signaling pathways in intestines with *dHNF4* suppression in ECs. Two different RNAi transgenes were used (*mex>dHNF4*$_i^{NIG/BDSC}$). Transcript levels are shown as relative to control levels (dotted line).

(D and E) *puc-lacZ* was used to score JNK activity in the intestine under different conditions. Antibody stains were used to visualize nuclear-targeted lacZ.

(D) Controls and *mex>dHNF4*$_i^{BDSC}$ animals were fed a standard diet or a lipid-free diet prepared with yeast extract.

(E) Control animals were fed a high-fat diet and midguts were counterstained with BODIPY (green) to mark neutral lipids. Left: representative pictures; R3 and R5 are indicated by closed and open arrowheads, respectively. Right: integrated *puc-lacZ* fluorescence intensity in R3 and R5. Fluorescence intensity was normalized to the surface of gut regions.

(A) Data are from three independent experiments. Dots: biological replicates, $27 > n > 17$. Line: median. (B–E) Data are from (B and C) one or (D and E) three to four experiments. Dots: biological replicates, (B and C) $n = 5$, (D and E) $29 > n > 23$, line: median, whiskers: minimum and maximum values. (A–E) $^{****}p < 0.0001$, $0.001 < {}^{**}p < 0.01$, and $0.01 < {}^{*}p < 0.05$; ns, no statistically significant difference (Mann-Whitney test). Asterisks indicate statistically significant differences with (A–C and E) controls or (D) *dHNF4* RNAi animals fed a standard diet.

See also Figure S6.

characterized.[10,52,53] Combined with a better understanding of the role of HNF4 in the intestine, these compounds could enable therapeutic control of gut function by harnessing the functions of this NR.

## Inter-organ communication controls intestinal lipid handling in *Drosophila*

Another pressing question in the field is whether intestinal lipid handling is under peripheral control.[2] We show that in *Drosophila*, hepatocyte-like cells suppress lipid retention in ECs (Figures 5 and S5). Our data support the model that dHNF4 promotes ImpL2 expression in oenocytes, which remotely activates Foxo and suppresses lipid retention in ECs (Figures 5B–5D). Given the well-established links between Foxo and lipolysis, this transcription factor may act through specific lipases, such as ATGL/brummer, to support continuous LD mobilization in epithelial cells (Figure S5H).[41] Foxo and dHNF4 may thus control the fate of dietary lipids in ECs by regulating

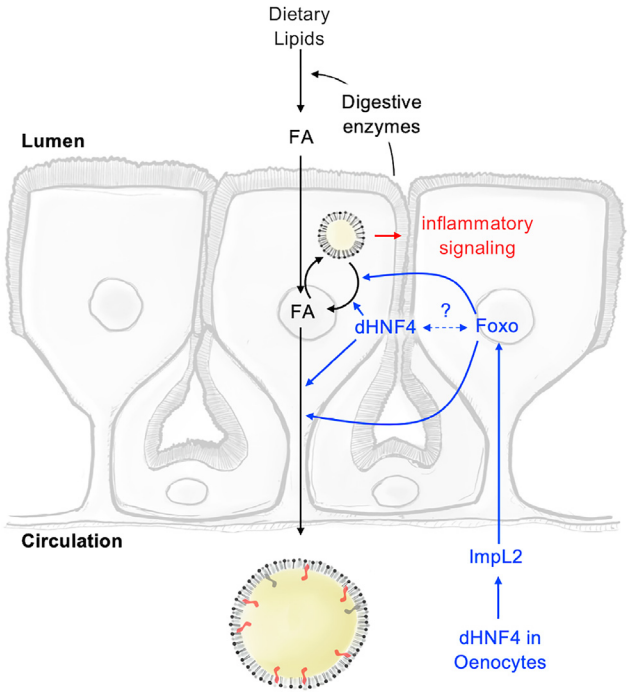


**Figure 7. *Drosophila* HNF4 acts in specialized ECs and hepatocyte-like cells to coordinate a switch between lipid storage and export in the gut**

dHNF4 controls the fate of dietary FAs after their absorption in interstitial cells: it suppresses their storage in cytoplasmic LDs, thereby promoting their export as lipoproteins. dHNF4 also acts in peripheral tissues to suppress lipid storage in interstitial cells. dHNF4 promotes the expression of ImpL2 in oenocytes. ImpL2 remotely activates Foxo signaling in interstitial cells, which suppresses LD accumulation in these cells. Future studies are needed to determine whether Foxo interacts with dHNF4 to promote LD mobilization in ECs. Disruption of the crosstalk between interstitial cells and oenocytes leads to aberrant accumulation of LDs in interstitial cells, which in turn can activate inflammatory signaling.

similar mechanisms. Further investigation is needed to determine if they exert these roles through functional interactions (Figure 7). On a broader perspective, our studies shed light on complex multiorgan interactions that fine-tune the function of the gut to meet the changing nutritional needs of the organism.

## Two different EC subtypes absorb dietary lipids and export them to peripheral tissues

*Drosophila* have been used for decades in metabolic research, but fundamental aspects of their physiology remain to be elucidated. Our study identifies key mechanisms that support nutrition in these invertebrates. We show that two EC subtypes, the ICs and R5 ECs, are in charge of lipid uptake and export. These cells, however, may use different strategies to fulfill this role. In particular, the physical interaction between ICs and copper cells suggests functional complementarity between these EC subtypes (Figure 2D). In addition to killing microbes, luminal acidification by copper cells could support the function of digestive enzymes that are analogs of the gastric lipase.[24–26,54,55] In contrast, the neutral to alkaline pH of R5 would be optimal for enzymes related to mammalian pancreatic lipases.[54,55] Knowing that gastric and pancreatic lipases act on different substrates, R3 and R5 could be specialized for the uptake of different lipid species. Along these lines, ectopic LDs formed upon the suppression of the lysosomal sterol esterase LipA could contain high levels of sterols, which are essential nutrients in *Drosophila* (Figure S4M). Future studies are needed to determine if ICs are specialized for the uptake and export of sterols and whether this function contributes to their recently described role in supporting growth and maturation.[27]

## A subset of ECs store lipids but do not export them

Our data suggest that specific EC populations rely on circulating lipoproteins to accumulate lipids (Figure 4B). This observation supports the "dual-track hypothesis," according to which ECs perform basolateral lipid transport for storage purposes.[1] Future studies in *Drosophila* may elucidate the physiological roles of basolateral lipid transport and fat storage in ECs.[1] These stores could be mobilized during nutritional stress, with R2 and R4 ECs playing a role similar to that of adipocytes. Along these lines, gut-derived citrate supports sperm production in testes.[56,57] Mobilization of intestinal lipid stores could ensure a continuous citrate supply and the maintenance of reproductive function despite nutrient scarcity. In parallel, we show that when *dHNF4* is silenced in ECs, lipids are retained in the gut at the expense of the thorax, which contains adipose tissue and flight muscles(Figures S4F and S4H). Gut-derived lipids may therefore support the high energetic demands of flight. EC lipid stores may also support gut physiology under adverse conditions. The intestinal epithelium produces reactive oxygen species via the dual oxidase DUOX to eliminate pathogenic microorganisms, a process that is dependent on lipolysis.[58] In parallel, epithelial regeneration relies on stem cell proliferation and their differentiation into mature ECs.[20] Knowing that stem cell maintenance is dependent on β-oxidation,[12] the release of free FAs from neighboring ECs may support regenerative mechanisms. Further studies are needed to test these hypotheses in *Drosophila* and determine whether "adipo-enterocytes" are specific to insects or more widespread in animals.

## Intestinal lipid overload is associated with inflammatory signaling

The idea of interfering with intestinal lipid absorption to combat obesity emerged in the 90s but has not led to significant therapeutic advances. Orlistat, for example, has been used for decades because of its suppressive effect on digestive lipase activity but has little effect on body weight.[2] Direct interference with lipid export in ECs seems an attractive strategy for weight control, but we show that it could have dramatic consequences. In particular, lipid retention in ECs is associated with cellular stress and production of inflammatory cytokines, which could be triggered by lipotoxicity and oxidative cell damage (Figure 6). A high-fat diet induces JNK signaling in wild-type intestines, and interestingly, this pathway is activated in steatotic ECs but also in their lean neighbors (Figure 6E, right image). Therefore, steatosis could also trigger stress signaling in a non-cell-autonomous manner. A possible mechanism underlying this effect is mechanical stress. Lipid retention is associated with dramatic changes in cell volume and morphology (Figures 2C and 2D). In R3, swollen, steatotic ICs appear to exert pressure on neighboring copper cells, leading to their

deformation (Figure 2C). Several cell populations in the midgut express the mechanosensitive ion channel piezo and are able to sense mechanical cues.[59] Knowing that Piezo1 can activate inflammatory signaling in mammals,[60,61] this stretch-activated channel could link steatosis and cell swelling with stress signaling in *Drosophila* intestines.

Feeding mice a high-fat diet is sufficient to induce intestinal inflammation, while colonic biopsies of patients with IBD often exhibit altered lipid levels.[62–65] Yet, whether specific pathways of lipid metabolism are responsible for triggering IBDs and the mechanisms involved in this relationship remain elusive. Our studies show that altering one of the most fundamental metabolic functions of ECs—to direct dietary fats for storage or export—recapitulates hallmark features of IBDs in *Drosophila*. Our studies therefore pave the way for a better understanding of the contribution of dietary fats in intestinal inflammation, as well as in the evolutionarily conserved mechanisms involved in this relationship.

### Limitations of the study

Our study shows that specific EC populations absorb dietary fats and export them to peripheral tissues. These populations may be specialized for the absorption of specific lipid classes, including sterols, for which *Drosophila* are auxotrophs. Regionalized studies are needed to determine these specificities. Important physiological changes occur in the female midgut after mating. How mating might affect the function of the EC populations described in this study remains to be investigated. Finally, our studies shed light on a physiological link between steatosis and inflammation in the gut, but the mechanisms involved in these relationships remain to be elucidated.

## RESOURCE AVAILABILITY

### Lead contact

Further information and requests for resources and reagents should be directed to and will be fulfilled by the lead contact, Gilles Storelli (gstorell@uni-koeln.de).

### Materials availability

All unique/stable reagents generated in this study are available from the lead contact with a completed materials transfer agreement.

### Data and code availability

- RNA-seq data have been deposited at GEO and are publicly available as of the date of publication. Accession numbers are listed in the key resources table.
- This paper does not report original code.
- Any additional information required to reanalyze the data reported in this paper is available from the lead contact upon request.

## ACKNOWLEDGMENTS

The authors thank M. Uhlirova for continuous support since the establishment of the Storelli lab; Flybase, the Vienna *Drosophila* Resource Center, the Bloomington *Drosophila* Stock Center, the Transgenic RNAi Project (TRiP), the NIG-FLY, B.A. Edgar, F. Leulier, and I. Miguel-Aliaga for sharing transgenic fly stocks; J. Mattila and A. Wodarz for sharing antibodies; S. Burgmer for providing support with confocal imaging; K. Emke for aiding with the analysis of cuticular hydrocarbons; the CECAD imaging facility (F. Babatz) and the Cologne Center for Genomics for technical support; and the Storelli lab members and F. Leulier for their comments on the manuscript. This research was supported by the NIH (R01DK108941, C.S.T.). "Gefördert durch die Deutsche Forschungsgemeinschaft (DFG) im Rahmen der Exzellenzstrategie des Bundes und der Länder - EXC 2030 - 390661388" (G.S.), and "Gefördert durch die Deutsche Forschungsgemeinschaft (DFG) - Projektnummer(470621046)" (G.S.).

## AUTHOR CONTRIBUTIONS

G.S. and C.S.T. supervised the work; G.S. and M.C.V. designed and interpreted experiments with input from F.L.M.z.A.; H.-J.N., G.S., M.C.V., F.L.M.z.A., and H.-J.N. performed the experiments; S.B. performed the lipidomic analyses; A.G. performed the transcriptomic analysis; G.L. generated the conditional *dHNF4* allele; J.B. analyzed cuticular hydrocarbons; and G.S. and M.C.V. wrote the paper with edits from C.S.T.

## DECLARATION OF INTERESTS

The authors declare no competing interests.

## STAR★METHODS

Detailed methods are provided in the online version of this paper and include the following:

- KEY RESOURCES TABLE
- EXPERIMENTAL MODEL AND STUDY PARTICIPANT DETAILS
  - *Drosophila melanogaster* strains
  - *Drosophila* strains were fed the following diets
- METHOD DETAILS
  - Conditional *dHNF4* allele
  - Lifespan studies
  - Oil Red O stains
  - Quantitative analysis of Oil Red O stains
  - Analysis of feeding behavior
  - Bodipy and phalloidin stains
  - Immunostaining
  - Imaging of transgenic fluorescent reporters
  - Quantification of foxo nuclear/cytoplasmic ratio
  - Quantification of puc-lacZ fluorescence signal
  - DNA extraction from tissues
  - RNA extraction from tissues and cDNA synthesis
  - Quantitative PCR (qPCR)
  - mRNA-sequencing
  - Transcriptomic analysis
  - Transmission electron microscopy
  - Sample preparation for lipidomic analyses
  - Hemolymph collection
  - Analysis of triacylglycerols by lipidomics
  - Analysis of hemolymph DAG by lipidomics
  - Fatty acid profiling
  - Enzymatic quantification of total TAG levels
  - Determination of intestinal lipase activity
  - Analysis of cuticular hydrocarbons (CHCs)
  - Information related to the experimental design
- QUANTIFICATION AND STATISTICAL ANALYSIS

## SUPPLEMENTAL INFORMATION

Supplemental information can be found online at https://doi.org/10.1016/j.celrep.2024.114693.

Received: March 26, 2024
Revised: July 15, 2024
Accepted: August 13, 2024

## REFERENCES


1. Cook, J.R., Kohan, A.B., and Haeusler, R.A. (2022). An Updated Perspective on the Dual-Track Model of Enterocyte Fat Metabolism. J. Lipid Res. *63*, 100278. https://doi.org/10.1016/j.jlr.2022.100278.
2. Wit, M., Trujillo-Viera, J., Strohmeyer, A., Klingenspor, M., Hankir, M., and Sumara, G. (2022). When fat meets the gut-focus on intestinal lipid handling in metabolic health and disease. EMBO Mol. Med. *14*, e14742. https://doi.org/10.15252/emmm.202114742.
3. Mansbach, C.M., and Siddiqi, S.A. (2010). The Biogenesis of Chylomicrons. Annu. Rev. Physiol. *72*, 315–333. https://doi.org/10.1146/annurev-physiol-021909-135801.
4. Affinati, A.H., Esfandiari, N.H., Oral, E.A., and Kraftson, A.T. (2019). Bariatric Surgery in the Treatment of Type 2 Diabetes. Curr. Diab. Rep. *19*, 156. https://doi.org/10.1007/s11892-019-1269-4.
5. Nguyen, N.T., and Varela, J.E. (2017). Bariatric surgery for obesity and metabolic disorders: state of the art. Nat. Rev. Gastroenterol. Hepatol. *14*, 160–169. https://doi.org/10.1038/nrgastro.2016.170.
6. Bridgham, J.T., Eick, G.N., Larroux, C., Deshpande, K., Harms, M.J., Gauthier, M.E.A., Ortlund, E.A., Degnan, B.M., and Thornton, J.W. (2010). Protein evolution by molecular tinkering: diversification of the nuclear receptor superfamily from a ligand-dependent ancestor. PLoS Biol. *8*, e1000497. https://doi.org/10.1371/journal.pbio.1000497.
7. Duda, K., Chi, Y.-I., and Shoelson, S.E. (2004). Structural Basis for HNF-4$\alpha$ Activation by Ligand and Coactivator Binding. J. Biol. Chem. *279*, 23311–23316. https://doi.org/10.1074/jbc.M400864200.
8. Wisely, G.B., Miller, A.B., Davis, R.G., Thornquest, A.D., Jr., Johnson, R., Spitzer, T., Sefler, A., Shearer, B., Moore, J.T., Miller, A.B., et al. (2002). Hepatocyte nuclear factor 4 is a transcription factor that constitutively binds fatty acids. Structure *10*, 1225–1234.
9. Yuan, X., Ta, T.C., Lin, M., Evans, J.R., Dong, Y., Bolotin, E., Sherman, M.A., Forman, B.M., and Sladek, F.M. (2009). Identification of an endogenous ligand bound to a native orphan nuclear receptor. PLoS One *4*, e5609. https://doi.org/10.1371/journal.pone.0005609.
10. Lee, S.-H., Veeriah, V., and Levine, F. (2021). Liver fat storage is controlled by HNF4$\alpha$ through induction of lipophagy and is reversed by a potent HNF4$\alpha$ agonist. Cell Death Dis. *12*, 603. https://doi.org/10.1038/s41419-021-03862-x.
11. Palanker, L., Tennessen, J.M., Lam, G., and Thummel, C.S. (2009). Drosophila HNF4 regulates lipid mobilization and beta-oxidation. Cell Metab. *9*, 228–239. https://doi.org/10.1016/j.cmet.2009.01.009.
12. Chen, L., Vasoya, R.P., Toke, N.H., Parthasarathy, A., Luo, S., Chiles, E., Flores, J., Gao, N., Bonder, E.M., Su, X., and Verzi, M.P. (2020). HNF4 Regulates Fatty Acid Oxidation and Is Required for Renewal of Intestinal Stem Cells in Mice. Gastroenterology *158*, 985–999.e9. https://doi.org/10.1053/j.gastro.2019.11.031.
13. Hayhurst, G.P., Lee, Y.H., Lambert, G., Ward, J.M., and Gonzalez, F.J. (2001). Hepatocyte nuclear factor 4alpha (nuclear receptor 2A1) is essential for maintenance of hepatic gene expression and lipid homeostasis. Mol. Cell Biol. *21*, 1393–1403. https://doi.org/10.1128/MCB.21.4.1393-1403.2001.
14. Yin, L., Ma, H., Ge, X., Edwards, P.A., and Zhang, Y. (2011). Hepatic hepatocyte nuclear factor 4alpha is essential for maintaining triglyceride and cholesterol homeostasis. Arterioscler. Thromb. Vasc. Biol. *31*, 328–336. https://doi.org/10.1161/ATVBAHA.110.217828.
15. Storelli, G., Nam, H.-J., Simcox, J., Villanueva, C.J., and Thummel, C.S. (2019). Drosophila HNF4 Directs a Switch in Lipid Metabolism that Supports the Transition to Adulthood. Dev. Cell *48*, 200–214.e6. https://doi.org/10.1016/j.devcel.2018.11.030.
16. Chen, L., Toke, N.H., Luo, S., Vasoya, R.P., Fullem, R.L., Parthasarathy, A., Perekatt, A.O., and Verzi, M.P. (2019). A reinforcing HNF4-SMAD4 feed-forward module stabilizes enterocyte identity. Nat. Genet. *51*, 777–785. https://doi.org/10.1038/s41588-019-0384-0.
17. Robinson-Rechavi, M., Escriva Garcia, H., and Laudet, V. (2003). The nuclear receptor superfamily. J. Cell Sci. *116*, 585–586. https://doi.org/10.1242/jcs.00247.
18. Girard, R., Tremblay, S., Noll, C., St-Jean, S., Jones, C., Gélinas, Y., Maloum-Rami, F., Perreault, N., Laplante, M., Carpentier, A.C., and Boudreau, F. (2022). The transcription factor hepatocyte nuclear factor 4A acts in the intestine to promote white adipose tissue energy storage. Nat. Commun. *13*, 224. https://doi.org/10.1038/s41467-021-27934-w.
19. Barry, W.E., and Thummel, C.S. (2016). The Drosophila HNF4 nuclear receptor promotes glucose-stimulated insulin secretion and mitochondrial function in adults. Elife *5*, e11183. https://doi.org/10.7554/eLife.11183.
20. Miguel-Aliaga, I., Jasper, H., and Lemaitre, B. (2018). Anatomy and Physiology of the Digestive Tract of Drosophila melanogaster. Genetics *210*, 357–396. https://doi.org/10.1534/genetics.118.300224.
21. Buchon, N., Osman, D., David, F.P.A., Fang, H.Y., Boquete, J.-P., Deplancke, B., and Lemaitre, B. (2013). Morphological and Molecular Characterization of Adult Midgut Compartmentalization in Drosophila. Cell Rep. *3*, 1725–1738. https://doi.org/10.1016/j.celrep.2013.04.001.
22. Marianes, A., and Spradling, A.C. (2013). Physiological and stem cell compartmentalization within the Drosophila midgut. Elife *2*, e00886. https://doi.org/10.7554/eLife.00886.
23. Dubreuil, R.R. (2004). Copper cells and stomach acid secretion in the Drosophila midgut. Int. J. Biochem. Cell Biol. *36*, 745–752. https://doi.org/10.1016/j.biocel.2003.07.004.
24. Storelli, G., Strigini, M., Grenier, T., Bozonnet, L., Schwarzer, M., Daniel, C., Matos, R., and Leulier, F. (2018). Drosophila Perpetuates Nutritional Mutualism by Promoting the Fitness of Its Intestinal Symbiont Lactobacillus plantarum. Cell Metab. *27*, 362–377.e8. https://doi.org/10.1016/j.cmet.2017.11.011.
25. Li, H., Qi, Y., and Jasper, H. (2016). Preventing Age-Related Decline of Gut Compartmentalization Limits Microbiota Dysbiosis and Extends Lifespan. Cell Host Microbe *19*, 240–253. https://doi.org/10.1016/j.chom.2016.01.008.
26. Overend, G., Luo, Y., Henderson, L., Douglas, A.E., Davies, S.A., and Dow, J.A.T. (2016). Molecular mechanism and functional significance of acid generation in the Drosophila midgut. Sci. Rep. *6*, 27242. https://doi.org/10.1038/srep27242.
27. Redhai, S., Pilgrim, C., Gaspar, P., Giesen, L.v., Lopes, T., Riabinina, O., Grenier, T., Milona, A., Chanana, B., Swadling, J.B., et al. (2020). An intestinal zinc sensor regulates food intake and developmental growth. Nature *580*, 263–268. https://doi.org/10.1038/s41586-020-2111-5.
28. Palm, W., Sampaio, J.L., Brankatschk, M., Carvalho, M., Mahmoud, A., Shevchenko, A., and Eaton, S. (2012). Lipoproteins in Drosophila melanogaster–assembly, function, and influence on tissue lipid composition. PLoS Genet. *8*, e1002828. https://doi.org/10.1371/journal.pgen.1002828.
29. Rommelaere, S., Boquete, J.-P., Piton, J., Kondo, S., and Lemaitre, B. (2019). The Exchangeable Apolipoprotein Nplp2 Sustains Lipid Flow and Heat Acclimation in Drosophila. Cell Rep. *27*, 886–899.e6. https://doi.org/10.1016/j.celrep.2019.03.074.
30. Parra-Peralbo, E., and Culi, J. (2011). Drosophila lipophorin receptors mediate the uptake of neutral lipids in oocytes and imaginal disc cells by an endocytosis-independent mechanism. PLoS Genet. *7*, e1001297. https://doi.org/10.1371/journal.pgen.1001297.
31. Rodríguez-Vázquez, M., Vaquero, D., Parra-Peralbo, E., Mejía-Morales, J.E., and Culi, J. (2015). Drosophila Lipophorin Receptors Recruit the Lipoprotein LTP to the Plasma Membrane to Mediate Lipid Uptake. PLoS Genet. *11*, e1005356. https://doi.org/10.1371/journal.pgen.1005356.
32. Hung, R.-J., Hu, Y., Kirchner, R., Liu, Y., Xu, C., Comjean, A., Tattikota, S.G., Li, F., Song, W., Ho Sui, S., and Perrimon, N. (2020). A cell atlas of the adult Drosophila midgut. Proc. Natl. Acad. Sci. USA *117*, 1514–1523. https://doi.org/10.1073/pnas.1916820117.
33. Sieber, M.H., and Thummel, C.S. (2012). Coordination of triacylglycerol and cholesterol homeostasis by DHR96 and the Drosophila LipA homolog

magro. Cell Metab. *15*, 122–127. https://doi.org/10.1016/j.cmet.2011.11.011.

34. Chng, W.-B.A., Sleiman, M.S.B., Schüpfer, F., and Lemaitre, B. (2014). Transforming growth factor β/activin signaling functions as a sugar-sensing feedback loop to regulate digestive enzyme expression. Cell Rep. *9*, 336–348. https://doi.org/10.1016/j.celrep.2014.08.064.
35. Mattila, J., Havula, E., Suominen, E., Teesalu, M., Surakka, I., Hynynen, R., Kilpinen, H., Väänänen, J., Hovatta, I., Käkelä, R., et al. (2015). Mondo-Mlx Mediates Organismal Sugar Sensing through the Gli-Similar Transcription Factor Sugarbabe. Cell Rep. *13*, 350–364. https://doi.org/10.1016/j.celrep.2015.08.081.
36. Gutierrez, E., Wiggins, D., Fielding, B., and Gould, A.P. (2007). Specialized hepatocyte-like cells regulate Drosophila lipid metabolism. Nature *445*, 275–280. https://doi.org/10.1038/nature05382.
37. Chatterjee, D., Katewa, S.D., Qi, Y., Jackson, S.A., Kapahi, P., and Jasper, H. (2014). Control of metabolic adaptation to fasting by dILP6-induced insulin signaling in Drosophila oenocytes. Proc. Natl. Acad. Sci. USA *111*, 17959–17964. https://doi.org/10.1073/pnas.1409241111.
38. Ghosh, A.C., Tattikota, S.G., Liu, Y., Comjean, A., Hu, Y., Barrera, V., Ho Sui, S.J., and Perrimon, N. (2020). Drosophila PDGF/VEGF signaling from muscles to hepatocyte-like cells protects against obesity. Elife *9*, e56969. https://doi.org/10.7554/eLife.56969.
39. Honegger, B., Galic, M., Köhler, K., Wittwer, F., Brogiolo, W., Hafen, E., and Stocker, H. (2008). Imp-L2, a putative homolog of vertebrate IGF-binding protein 7, counteracts insulin signaling in Drosophila and is essential for starvation resistance. J. Biol. *7*, 10. https://doi.org/10.1186/jbiol72.
40. Evdokimova, V., Tognon, C.E., Benatar, T., Yang, W., Krutikov, K., Pollak, M., Sorensen, P.H.B., and Seth, A. (2012). IGFBP7 binds to the IGF-1 receptor and blocks its activation by insulin-like growth factors. Sci. Signal. *5*, ra92. https://doi.org/10.1126/scisignal.2003184.
41. Wang, B., Moya, N., Niessen, S., Hoover, H., Mihaylova, M.M., Shaw, R.J., Yates, J.R., Fischer, W.H., Thomas, J.B., and Montminy, M. (2011). Characterization of a Hormone Dependent Module Regulating Energy Balance. Cell *145*, 596–606. https://doi.org/10.1016/j.cell.2011.04.013.
42. Puig, O., Marr, M.T., Ruhf, M.L., and Tjian, R. (2003). Control of cell number by Drosophila FOXO: downstream and feedback regulation of the insulin receptor pathway. Genes Dev. *17*, 2006–2020. https://doi.org/10.1101/gad.1098703.
43. Clarke, K.R. (1993). Non-parametric multivariate analyses of changes in community structure. Aust. J. Ecol. *18*, 117–143. https://doi.org/10.1111/j.1442-9993.1993.tb00438.x.
44. UK IBD Genetics Consortium; Barrett, J.C., Lee, J.C., Lees, C.W., Prescott, N.J., Anderson, C.A., Phillips, A., Wesley, E., Parnell, K., Zhang, H., et al. (2009). Genome-wide association study of ulcerative colitis identifies three new susceptibility loci, including the HNF4A region. Nat. Genet. *41*, 1330–1334. https://doi.org/10.1038/ng.483.
45. Marcil, V., Sinnett, D., Seidman, E., Boudreau, F., Gendron, F.P., Beaulieu, J.F., Menard, D., Lambert, M., Bitton, A., Sanchez, R., et al. (2012). Association between genetic variants in the HNF4A gene and childhood-onset Crohn's disease. Genes Immun. *13*, 556–565. https://doi.org/10.1038/gene.2012.37.
46. van Sommeren, S., Visschedijk, M.C., Festen, E.A.M., de Jong, D.J., Ponsioen, C.Y., Wijmenga, C., and Weersma, R.K. (2011). HNF4alpha and CDH1 are associated with ulcerative colitis in a Dutch cohort. Inflamm. Bowel Dis. *17*, 1714–1718. https://doi.org/10.1002/ibd.21541.
47. Kockel, L., Homsy, J.G., and Bohmann, D. (2001). Drosophila AP-1: lessons from an invertebrate. Oncogene *20*, 2347–2364. https://doi.org/10.1038/sj.onc.1204300.
48. Amoyel, M., and Bach, E.A. (2012). Functions of the Drosophila JAK-STAT pathway: Lessons from stem cells. JAK-STAT *1*, 176–183. https://doi.org/10.4161/jkst.21621.
49. Karsten, P., Häder, S., and Zeidler, M.P. (2002). Cloning and expression of Drosophila SOCS36E and its potential regulation by the JAK/STAT pathway. Mech. Dev. *117*, 343–346. https://doi.org/10.1016/s0925-4773(02)00216-2.
50. Ahn, S.H., Shah, Y.M., Inoue, J., Morimura, K., Kim, I., Yim, S., Lambert, G., Kurotani, R., Nagashima, K., Gonzalez, F.J., and Inoue, Y. (2008). Hepatocyte nuclear factor 4alpha in the intestinal epithelial cells protects against inflammatory bowel disease. Inflamm. Bowel Dis. *14*, 908–920. https://doi.org/10.1002/ibd.20413.
51. Darsigny, M., Babeu, J.-P., Dupuis, A.-A., Furth, E.E., Seidman, E.G., Lévy, E., Verdu, E.F., Gendron, F.-P., and Boudreau, F. (2009). Loss of hepatocyte-nuclear-factor-4alpha affects colonic ion transport and causes chronic inflammation resembling inflammatory bowel disease in mice. PLoS One *4*, e7609. https://doi.org/10.1371/journal.pone.0007609.
52. Kiselyuk, A., Lee, S.-H., Farber-Katz, S., Zhang, M., Athavankar, S., Cohen, T., Pinkerton, A.B., Ye, M., Bushway, P., Richardson, A.D., et al. (2012). HNF4α antagonists discovered by a high-throughput screen for modulators of the human insulin promoter. Chem. Biol. *19*, 806–818. https://doi.org/10.1016/j.chembiol.2012.05.014.
53. Lee, S.-H., Athavankar, S., Cohen, T., Piran, R., Kiselyuk, A., and Levine, F. (2013). Identification of alverine and benfluorex as HNF4α activators. ACS Chem. Biol. *8*, 1730–1736. https://doi.org/10.1021/cb4000986.
54. Acevedo-Fani, A., and Singh, H. (2022). Biophysical insights into modulating lipid digestion in food emulsions. Prog. Lipid Res. *85*, 101129. https://doi.org/10.1016/j.plipres.2021.101129.
55. Bauer, E., Jakob, S., and Mosenthin, R. (2005). Principles of Physiology of Lipid Digestion. Asian-Australas. J. Anim. Sci. *18*, 282–295. https://doi.org/10.5713/ajas.2005.282.
56. Hudry, B., de Goeij, E., Mineo, A., Gaspar, P., Hadjieconomou, D., Studd, C., Mokochinski, J.B., Kramer, H.B., Plaçais, P.-Y., Preat, T., and Miguel-Aliaga, I. (2019). Sex Differences in Intestinal Carbohydrate Metabolism Promote Food Intake and Sperm Maturation. Cell *178*, 901–918.e16. https://doi.org/10.1016/j.cell.2019.07.029.
57. François, C.M., Pihl, T., Dunoyer de Segonzac, M., Hérault, C., and Hudry, B. (2023). Metabolic regulation of proteome stability via N-terminal acetylation controls male germline stem cell differentiation and reproduction. Nat. Commun. *14*, 6737. https://doi.org/10.1038/s41467-023-42496-9.
58. Lee, K.-A., Cho, K.-C., Kim, B., Jang, I.-H., Nam, K., Kwon, Y.E., Kim, M., Hyeon, D.Y., Hwang, D., Seol, J.-H., and Lee, W.J. (2018). Inflammation-Modulated Metabolic Reprogramming Is Required for DUOX-Dependent Gut Immunity in Drosophila. Cell Host Microbe *23*, 338–352.e5. https://doi.org/10.1016/j.chom.2018.01.011.
59. He, L., Si, G., Huang, J., Samuel, A.D.T., and Perrimon, N. (2018). Mechanical regulation of stem-cell differentiation by the stretch-activated Piezo channel. Nature *555*, 103–106. https://doi.org/10.1038/nature25744.
60. Zhao, F., Zhang, L., Wei, M., Duan, W., Wu, S., and Kasim, V. (2022). Mechanosensitive Ion Channel PIEZO1 Signaling in the Hall-Marks of Cancer: Structure and Functions. Cancers *14*, 4955. https://doi.org/10.3390/cancers14194955.
61. Liu, H., Hu, J., Zheng, Q., Feng, X., Zhan, F., Wang, X., Xu, G., and Hua, F. (2022). Piezo1 Channels as Force Sensors in Mechanical Force-Related Chronic Inflammation. Front. Immunol. *13*, 816149. https://doi.org/10.3389/fimmu.2022.816149.
62. Diab, J., Hansen, T., Goll, R., Stenlund, H., Ahnlund, M., Jensen, E., Moritz, T., Florholmen, J., and Forsdahl, G. (2019). Lipidomics in Ulcerative Colitis Reveal Alteration in Mucosal Lipid Composition Associated With the Disease State. Inflamm. Bowel Dis. *25*, 1780–1787. https://doi.org/10.1093/ibd/izz098.
63. Fernández-Bañares, F., Esteve-Comas, M., Mañé, J., Navarro, E., Bertrán, X., Cabré, E., Bartolí, R., Boix, J., Pastor, C., and Gassull, M.A. (1997). Changes in mucosal fatty acid profile in inflammatorybowel disease and in experimental colitis: a common response to bowel inflammation. Clin. Nutr. *16*, 177–183.
64. Shores, D.R., Binion, D.G., Freeman, B.A., and Baker, P.R.S. (2011). New Insights into the Role of Fatty Acids in the Pathogenesis and Resolution of

Inflammatory Bowel Disease. Inflamm. Bowel Dis. *17*, 2192–2204. https://doi.org/10.1002/ibd.21560.

65. Cani, P.D., Amar, J., Iglesias, M.A., Poggi, M., Knauf, C., Bastelica, D., Neyrinck, A.M., Fava, F., Tuohy, K.M., Chabo, C., et al. (2007). Metabolic endotoxemia initiates obesity and insulin resistance. Diabetes *56*, 1761–1772. https://doi.org/10.2337/db06-1491.
66. Gratz, S.J., Ukken, F.P., Rubinstein, C.D., Thiede, G., Donohue, L.K., Cummings, A.M., and O'Connor-Giles, K.M. (2014). Highly specific and efficient CRISPR/Cas9-catalyzed homology-directed repair in Drosophila. Genetics *196*, 961–971. https://doi.org/10.1534/genetics.113.160713.
67. Itskov, P.M., Moreira, J.-M., Vinnik, E., Lopes, G., Safarik, S., Dickinson, M.H., and Ribeiro, C. (2014). Automated monitoring and quantitative analysis of feeding behaviour in Drosophila. Nat. Commun. *5*, 4560. https://doi.org/10.1038/ncomms5560.
68. Zhou, Y., Zhou, B., Pache, L., Chang, M., Khodabakhshi, A.H., Tanaseichuk, O., Benner, C., and Chanda, S.K. (2019). Metascape provides a biologist-oriented resource for the analysis of systems-level datasets. Nat. Commun. *10*, 1523. https://doi.org/10.1038/s41467-019-09234-6.
69. Kumar, V., Bouameur, J.-E., Bär, J., Rice, R.H., Hornig-Do, H.-T., Roop, D.R., Schwarz, N., Brodesser, S., Thiering, S., Leube, R.E., et al. (2015). A keratin scaffold regulates epidermal barrier formation, mitochondrial lipid composition, and activity. J. Cell Biol. *211*, 1057–1075. https://doi.org/10.1083/jcb.201404147.
70. Turpin-Nolan, S.M., Hammerschmidt, P., Chen, W., Jais, A., Timper, K., Awazawa, M., Brodesser, S., and Brüning, J.C. (2019). CerS1-Derived C18:0 Ceramide in Skeletal Muscle Promotes Obesity-Induced Insulin Resistance. Cell Rep. *26*, 1–10.e7. https://doi.org/10.1016/j.celrep.2018.12.031.
71. Özbalci, C., Sachsenheimer, T., and Brügger, B. (2013). Quantitative analysis of cellular lipids by nano-electrospray ionization mass spectrometry. Methods Mol. Biol. *1033*, 3–20. https://doi.org/10.1007/978-1-62703-487-6_1.
72. Ejsing, C.S., Sampaio, J.L., Surendranath, V., Duchoslav, E., Ekroos, K., Klemm, R.W., Simons, K., and Shevchenko, A. (2009). Global analysis of the yeast lipidome by quantitative shotgun mass spectrometry. Proc. Natl. Acad. Sci. USA *106*, 2136–2141. https://doi.org/10.1073/pnas.0811700106.
73. Hellmuth, C., Weber, M., Koletzko, B., and Peissner, W. (2012). Nonesterified fatty acid determination for functional lipidomics: comprehensive ultrahigh performance liquid chromatography-tandem mass spectrometry quantitation, qualification, and parameter prediction. Anal. Chem. *84*, 1483–1490. https://doi.org/10.1021/ac202602u.
74. Oksanen, J., Blanchet, F.G., Kindt, R., Legendre, P., Minchin, P.R., O'Hara, R.B., Simpson, G.L., Sólymos, P., Stevens, M.H.H., and Wagner, H. (2012). Vegan: Community Ecology Package. https://doi.org/10.32614/CRAN.package.vegan.

## STAR★METHODS

### KEY RESOURCES TABLE

| REAGENT or RESOURCE | SOURCE | IDENTIFIER |
|---|---|---|
| Antibodies | | |
| **Anti-aPKC (PRKC zeta (C-20))** | Santa Cruz Biotechnology | RRID: AB_2300359 |
| **Anti-Armadillo (Mouse Anti-*Drosophila* Armadillo Protein Monoclonal Antibody)** | DSHB | RRID: AB_528089 |
| **Anti-beta-Gal (Anti-beta-galactosidase, purified monoclonal antibody)** | Promega | RRID: AB_430877 |
| **Anti-dHNF4 (Affinity-purified guinea pig anti dHNF4 antibody)** | Palanker et al. (2009)[11] | N/A |
| **Anti-Foxo (Anti-N-terminal dFoxo)** | Puig et al. (2003)[42] | N/A |
| **Anti-Guinea Pig (Cy™3 AffiniPure™ Donkey Anti-Guinea Pig IgG (H+L))** | Jackson Immuno | RRID: AB_2340460 |
| **Anti-Mouse (Goat anti-Mouse IgG (H+L) Highly Cross-Adsorbed Secondary Antibody, Alexa Fluor™ 633)** | Thermo Fisher Scientific | RRID: AB_2535719 |
| **Anti-pHH3 (Anti-phospho Histone H3 (Ser 10))** | Merck | RRID: AB_310177 |
| **Anti-Prospero (Mouse Anti-*Drosophila* Prospero Protein Monoclonal Antibody)** | DSHB | RRID: AB_528440 |
| **Anti-Rabbit (Cy™3 AffiniPure™ Donkey Anti-Rabbit IgG (H+L))** | Jackson Immuno | RRID: AB_2307443 |
| Chemicals, peptides, and recombinant proteins | | |
| **Active dry yeast** | Bäckerei Spiegelhauer | Cat#1278 |
| **Alexa Fluor 555 Phalloidin** | Cell Signaling | Cat#8953S |
| **BODIPY 493/503** | Invitrogen | Cat#D3922 |
| **DSS** | MP Biomedical | Cat#101516 |
| **Methyl 4-hydroxybenzoate sodium salt** | VWR | Cat#235145000 |
| **Normal donkey serum** | Biozol | Cat#LIN-END9010-10 |
| **Oil red O** | Sigma-Aldrich | Cat#O0625-100G |
| **Paraquat** | Sigma-Aldrich | Cat#856177 |
| **Soy phospholipids** | Sigma Aldrich | Cat#11145-50G |
| **Sucrose** | Merck | Cat#1076875000 |
| **Water-soluble yeast Extract** | Carl Roth | Cat#2363.1 |
| Critical commercial assays | | |
| **Bio-Rad Protein Assay Dye** | Bio-Rad | Cat#5000006 |
| **DNeasy Blood & Tissue Kit** | Qiagen | Cat#69504 |
| **Free glycerol reagent** | Sigma-Aldrich | Cat#F6428-40ML |
| **GoTaq qPCR Master Mix** | Promega | Cat#A6001 |
| **Lipase Activity Assay Kit** | Sigma-Aldrich | Cat#MAK047 |
| **qScript cDNA Supermix** | Quantabio | Cat#733-1178 |
| **Reliaprep RNA tissue miniprep system** | Promega | Cat#Z6112 |
| **Triglyceride reagent** | Sigma-Aldrich | Cat#T2449-10ML |
| Deposited data | | |
| **Raw and analyzed mRNA-sequencing data** | This paper | GEO: GSE271746 |
| Experimental models: Organisms/strains | | |
| ***D. melanogaster: 10XStat92E-GFP: w[1118]; P{w[+mC] = 10XStat92E-GFP}1*** | BDSC | RRID: BDSC_26197 |
| ***D. melanogaster: caudal-GAL4*** | F. Leulier | N/A |
| ***D. melanogaster: Cg$^{ts}$>: w[*]; Cg-GAL4/CyO; P{tubP-GAL80ts}/TM3*** | K. Beebe | N/A |

(*Continued on next page*)

*Continued*

| REAGENT or RESOURCE | SOURCE | IDENTIFIER |
|---|---|---|
| ***D. melanogaster: dHNF4$^{\Delta 17}$: w[*]; dHNF4[17]/CyO*** | Palanker et al. (2009)[11] | N/A |
| ***D. melanogaster: dHNF4$^{\Delta 33}$: w[*]; Hnf4[33]/CyO*** | Palanker et al. (2009)[11] | RRID: BDSC_43643 |
| ***D. melanogaster: EP$^{2449}$: w[1118]; P{w[+mC] = EP}Hnf4[EP2449]*** | Palanker et al. (2009)[11] | RRID: BDSC_17249 |
| ***D. melanogaster: Esg-GAL4 UAS-GFP: w[*]; P{w[+mW.hs] = GawB}NP5130 P{w[+mC] = UAS-GFP.U}2/CyO; P{y[+t7.7] w[+mC] = UAS-3xFLAG.dCas9.VPR}attP2*** | BDSC | RRID: BDSC_67054 |
| ***D. melanogaster: Hodor-GAL4: w[*]; M{pHCl-2-GAL4.R}/CyO*** | Redhai et al. (2020)[27] | N/A |
| ***D. melanogaster: KG$^{08976}$: y[1]; P{y[+mDint2] w[BR.E.BR] = SUPor-P}Hnf4[KG08976]*** | Palanker et al. (2009)[11] | RRID: BDSC_16471 |
| ***D. melanogaster: Mal-A7-GAL4: y$^{1}$ w*; Mi{Trojan-GAL4.2}Mal-A7$^{MI00819\text{-}TG4.2}$*** | BDSC | RRID: BDSC_76622 |
| ***D. melanogaster: mex-GAL4 (II): w[1118]; P{w[+mC] = mex1-GAL4.2.1}10-8*** | BDSC | RRID: BDSC_ 91368 |
| ***D. melanogaster: mex-GAL4 (X): P{w[+mC] = mex1-GAL4.2.1}9-1, y[1] w[1118]*** | BDSC | RRID: BDSC_ 91367 |
| ***D. melanogaster: PromE$^{ts}$>: P{w[+mC] = Desat1-GAL4.E800}2M, P{w[+mC] = tubP-GAL80[ts]}20*** | BDSC | RRID: BDSC_65406 |
| ***D. melanogaster: puc-lacZ: P{ry[+t7.2] = lArB}puc[A251.1F3] ry[506]/TM3, Sb[1]*** | BDSC | RRID: BDSC_11173 |
| ***D. melanogaster: UAS-attp40: y[1] v[1]; P{y[+t7.7] = CaryP}Msp300[attP40]*** | BDSC | RRID: BDSC_36304 |
| ***D. melanogaster: UAS-ATGL/bmm: w*; UAS-ATGL/bmm*** | C. Thummel | N/A |
| ***D. melanogaster: UAS-CG2772$_i^{VDRC}$: P{KK104580}VIE-260B*** | VDRC/KK | RRID: SCR_013805; Cat#105255 |
| ***D. melanogaster: UAS-CG31089$_i^{VDRC}$: w[1118]; P{GD287}v11695*** | VDRC/GD | RRID: SCR_013805; Cat#11695 |
| ***D. melanogaster: UAS-CG31091$_i^{VDRC}$: w[1118]; P{GD286}v33084*** | VDRC/GD | RRID: SCR_013805; Cat#33084 |
| ***D. melanogaster: UAS-CG3635$_i^{VDRC}$: w[1118]; P{GD1804}v37135*** | VDRC/GD | RRID: SCR_013805; Cat#37135 |
| ***D. melanogaster: UAS-dHNF4$_i^{BDSC}$: w[*]; P{y[+t7.7] w[+mC] = UAS-Hnf4.RNAi}attP16/CyO*** | BDSC | RRID: BDSC_44398 |
| ***D. melanogaster: UAS-dHNF4$_i^{NIG}$: w[*];; NIG9310R-2/TM3, sb, ser*** | NIG | NIG#9310R-2 |
| ***D. melanogaster: UAS-dHNF4$_i^{TRIP}$: y[1] sc[*] v[1] sev[21]; P{y[+t7.7] v[+t1.8] = TRiP.HMC05862}attP40*** | BDSC | RRID: BDSC_64988 |
| ***D. melanogaster: UAS-foxo$_i^{VDRC}$: P{KK108485}VIE-260B*** | BDSC/KK | RRID: SCR_13805; Cat#106097 |
| ***D. melanogaster: UAS-GFP.nls: w[1118]; P{w[+mC] = UAS-GFP.nls}14*** | BDSC | RRID: BDSC_4775 |
| ***D. melanogaster: UAS-LipA$_i^{VDRC}$: P{KK103835}VIE-260B*** | VDRC/KK | RRID: SCR_013805; Cat#109706 |
| ***D. melanogaster: UAS-lpp$_i^{VDRC}$: P{KK106311}VIE-260B*** | VDRC/KK | RRID: SCR_013805; Cat#100944 |
| ***D. melanogaster: UAS-LpR1$_i^{VDRC}$: P{KK110259}VIE-260B*** | VDRC/KK | RRID: SCR_013805; Cat#106364 |
| ***D. melanogaster: UAS-LpR2$_i^{VDRC}$: w[1118]; P{GD10161}v25684*** | VDRC/GD | RRID: SCR_013805; Cat#25684 |
| ***D. melanogaster: UAS-Ltp$_i^{VDRC}$: P{VSH330511}attP40*** | VDRC | RRID: SCR_013805; Cat#330511 |
| ***D. melanogaster: UAS-Mtp$_i^{VDRC}$: P{KK101495}VIE-260B*** | VDRC/KK | RRID: SCR_013805; Cat#110414 |
| ***D. melanogaster: UAS-Nplp2$_i^{VDRC}$: w[1118]; P{GD4710}v15305*** | VDRC/GD | RRID: SCR_013805; Cat#15305 |
| ***D. melanogaster: UAS-Nplp2$_i^{VDRC\#2}$: w[1118]; P{GD4710}v15306/TM3*** | VDRC/GD | RRID: SCR_013805; Cat#15306 |
| ***D. melanogaster: UAS-Plc21c$_i^{VDRC}$: w[1118]; P{GD11359}v26557*** | VDRC/GD | RRID: SCR_013805; Cat#26557 |
| ***D. melanogaster: UAS-Pld$_i^{VDRC}$: w[1118]; P{GD7487}v38626*** | VDRC/GD | RRID: SCR_013805; Cat#38626 |
| ***D. melanogaster: UAS-Rab5$_i^{VDRC}$: w[1118]; P{KK102895}VIE-260B*** | VDRC/KK | RRID: SCR_013805;Cat #103945 |
| ***D. melanogaster: UAS-Sturkopf$_i^{VDRC}$: P{KK108771}VIE-260B*** | VDRC/KK | RRID: SCR_013805; Cat#105945 |
| ***D. melanogaster: y[1] M{GFP[E.3xP3] = vas-Cas9.RFP-}ZH-2A w[1118]*** | BDSC | RRID: BDSC_55821 |
| ***D. melanogaster: yw, hs-Flp, UAS-GFP; FRT-HNF4-FRT*** | This paper | N/A |

(*Continued on next page*)

*Continued*

| REAGENT or RESOURCE | SOURCE | IDENTIFIER |
|---|---|---|
| Oligonucleotides | | |
| **Oligonucleotides for qPCR, see** Table S4 | IDT | N/A |
| Software and algorithms | | |
| **Graphpad prism 8** | Graphpad software | https://www.graphpad.com/scientific-software/prism/ |
| **ImageJ** | NIH Image | https://imagej.net/ImageJ |
| **SkanIt** | ThermoFisher scientific | https://www.thermofisher.com |
| **Zen** | Zeiss | https://www.zeiss.com/microscopy/en/products/software/light-microscopy-software.html |

## EXPERIMENTAL MODEL AND STUDY PARTICIPANT DETAILS

### *Drosophila melanogaster* strains

Unless otherwise stated, 7- to 10-day-old adult males were used for experiments. Detailed lists of strains and genotypes are provided in the key resources table and Table S3, respectively. Fly strains were routinely kept at room temperature on a diet composed of yeast, cornmeal, corn syrup and malt. For experiments, parents were crossed in polypropylene bottles (Kisker Biotech, 789022B) containing our standard diet (recipe below) at room temperature. Progenies were collected shortly after adult emergence and transferred to polystyrene vials (Kisker Biotech, 789009) containing our standard diet at a density of 10–20 animals/vial. Adults were then kept at 25°C with a 12-h light cycle. For experiments involving adult-specific transgene expression with temperature-controlled drivers, animals were transferred from room temperature to 29°C after adult eclosion. For adult-specific deletion of the *dHNF4* locus, animals carrying a *hs-FLP* transgene and a transheterozygous combination of a *dHNF4* null allele and a *dHNF4* conditional allele were allowed to develop until six days after adult eclosion. They were then subjected to two sequential 1-h heat pulses at 37°C separated by 24 h at 25°C. Animals were kept for an additional seven days at 25°C until experiments were performed. More details are provided in the section "Conditional *dHNF4* allele".

### *Drosophila* strains were fed the following diets

Standard diet: For 1 L: 80 g active dry yeast (Bäckerei Spiegelhauer, Cat#1278), 10 g agar (Fisher Scientific, BP1423-2). The ingredients were mixed with water and brought to boil for 10 min. After cooling, 4 mL of 99% propionic acid and 5.2 g of methyl 4-hydroxybenzoate sodium salt (VWR, Cat#235145000) were added to the mixture and the solution was poured into vials or bottles.

Standard diet with Dextran Sodium Sulfate (DSS): same recipe as above, DSS (MP Biomedical, Cat#101516, average molecular weight: 8000 Da) was added at a concentration of 5% weight/volume after cooling.

Standard diet with paraquat: same recipe as above, paraquat (Sigma-Aldrich, Cat#856177) was added at a concentration of 5 mM after cooling.

Yeast extract diet (lipid-free): same recipe as above, but active dry yeast was replaced with water soluble yeast extract (Carl Roth, 2363.1).

Diet with lipid-free yeast: same recipe as above, but active dry yeast was replaced with yeast that has undergone lipid extraction.

For lipid extraction in yeast, 10 g of active dry yeast (Bäckerei Spiegelhauer, Cat#1278) was incubated in a solution of chloroform-methanol (2:1, v/v, Carl Roth 4423.1 and AE01.1, respectively) in a 50 mL tube. The tubes were vortexed vigorously for 10 min and centrifuged for 3 min at 3220 x g. The supernatant was discarded and chloroform-methanol extraction was repeated 4 more times. Lipid-extracted yeasts were allowed to dry under a chemical hood until complete evaporation of chloroform and methanol. Lipid-free yeasts were then used to prepare *Drosophila* diets as described above.

Sugar diet: same recipe as above, but sucrose (Merck, Cat#1076875000) was added at a concentration of 15% weight/volume.

High-fat diet: same recipe as above, but soy phospholipids (Sigma Aldrich 11145-50G) were added at a concentration of 10% weight/volume. Vials were kept horizontal to prevent flies from sticking to the high-fat diet. A piece of wet Whatman paper was added to the vials to facilitate hydration.

## METHOD DETAILS

### Conditional *dHNF4* allele

Two FRT sequences were introduced into the *dHNF4* locus with CRISPR-Cas9 technology.[66] We targeted a genomic region extending from nucleotides 8, 686,152 to 8,691,550 on the left arm of the second chromosome. The sequence of this region is shown in (Figure S2), with the FRT sequences highlighted in yellow and the *3xPax3-DsRed* reporter insertion in red font. The *3xPax3-DsRed*

reporter is transcribed off the opposite strand from *dHNF4* so that it does not interfere with *dHNF4* transcript elongation. A plasmid carrying this sequence was injected into $y^1$ *M(vas-Cas9.RFP)ZH-2A* $w^{1118}$ embryos (RRID: BDSC_55821) together with plasmids expressing the following guide RNAs: 5′ guide GTAACATTTAAGACTGTGTCAGG and 3′ guide GATCAGGGTTACGTTCTAAGTGG. Integrants were selected based on dsRed expression in the adult eye. Stocks were established from single males and sequenced to confirm the accurate integration of the FRT sequences. FLP-mediated excision of the intervening sequences was assayed by qPCR analysis of *dHNF4* genomic sequence and *dHNF4* transcript levels (Figure S2).

### Lifespan studies

Animals were collected at adult eclosion and transferred to polystyrene vials containing our standard diet or a diet supplemented with DSS or paraquat at a density of 10–15 males per vial at 25°C. Vials were closed with a dense weave cellulose stopper (Flugs; Kisker Biotech, Cat# 789035) to reduce water evaporation from food. Animals were transferred weekly to vials containing fresh media and lethality was assayed every one to two days. Experiments were repeated two to three times and a representative experiment was selected for the figures.

### Oil Red O stains

Intestines were dissected in PBS and fixed in 4% paraformaldehyde for 1 h at room temperature. Tissues were then washed twice in PBS and twice in propylene glycol before being incubated for 1 h at 37°C in 0.5% Oil red O (Sigma Aldrich, O0625-100G) in propylene glycol. Tissues were then washed twice in propylene glycol, twice in PBS and mounted in a drop of glycerol on a microscopy slide. A coverslip was then deposited on top of the dissected tissues before imaging by bright field microscopy. Oil red O stains were performed on two to three independent sets of 10–15 tissues. A representative image is shown in the figures.

### Quantitative analysis of Oil Red O stains

Bright field images were opened as TIFF files in ImageJ, converted to RGB, then to 8-bit, and inverted. The polygon tool was used to select regions of interest in the intestine. A threshold was manually applied to selectively outline the portions stained with Oil Red O in these regions and calculate their area. The area stained with Oil Red O was then divided by the total area of the regions of interest to determine the "% Area occupied by lipids".

### Analysis of feeding behavior

Feeding behavior was analyzed using the FlyPAD system.[67] The two electrodes in each arena were loaded with 5 μL of standard diet or 1% agar in water, respectively. Adult males were transferred to the arenas and sips on standard diet were recorded for 1 h at 25°C or 29°C, depending on the genotype. Three independent experiments were performed with 12 flies per genotype. Spill control was set to 0.5 to remove arenas where the signal is saturated more than 50% of the time. Global non-eaters were excluded from the analysis.

### Bodipy and phalloidin stains

After fixation and immunostaining (see details below), tissues were incubated in the dark in 2 μg/mL BODIPY 493/503 (Invitrogen, D3922) and 33 nM Alexa Fluor 555 Phalloidin (Cell Signaling, 8953S) in PBS for 1 h. After incubation, tissues were washed three times in PBS and mounted in RotiMount FluorCare DAPI mounting medium (Carl Roth, HP20.1). Pictures were taken with an LSM 980 with Airyscan 2 confocal laser scanning microscope.

### Immunostaining

Tissues were dissected in PBS, fixed in 4% paraformaldehyde for 1 h at room temperature, and rinsed three times in PBS 0.5% Triton X-100 (PBST). Samples were then incubated in blocking buffer (5% normal donkey serum (Biozol, LIN-END9010-10) in PBST) for 12 h and incubated in primary antibody diluted in blocking buffer for at least 12 h at 4°C. Tissues were then rinsed twice and washed for 1 h in PBST. They were incubated in secondary antibody (diluted in blocking buffer) for 2 to 3 h in the dark and at room temperature. Following dilutions were used: Anti-aPKC, beta-Gal, dHNF4: 1:100, Armadillo: 1:20, Foxo: 1:200, pHH3, Guinea Pig, Rabbit, Mouse: 1:500, Prospero: 1:5. Tissues were then rinsed twice in PBST and washed in PBS for 1 h before mounting in RotiMount FluorCare DAPI mounting medium (Carl Roth, HP20.1). Tissues were imaged using an Olympus BX53 fluorescence microscope or an LSM 980 with Airyscan 2 confocal laser scanning microscope. Two to three independent stains were performed on sets of 10–15 tissues. A representative image is shown in the figures. For quantification of pHH3-positive cells, cells were manually counted for each midgut using an Olympus BX53 fluorescence microscope. Three independent quantifications were performed.

### Imaging of transgenic fluorescent reporters

Tissues expressing GFP under the control of different GAL4 drivers were rapidly dissected in PBS, fixed in 4% paraformaldehyde for 30 min at room temperature, rinsed three times in PBS and mounted in RotiMount FluorCare DAPI mounting medium (Carl Roth, HP20.1). Tissues were directly imaged after mounting.

### Quantification of foxo nuclear/cytoplasmic ratio

Midguts were stained with anti-Foxo antibody and counterstained with DAPI. A portion of the R2 proximal to the R3 was imaged using an Olympus BX53 widefield fluorescence microscope. We imaged the R2 rather than the R3 for these analyses because we observed a strong, non-specific signal on apical domain of the copper cells when performing anti-Foxo stains, presumably due to non-specific binding of the antibodies. The complex three-dimensional structure of the R3 also limits the number of nuclei that can be captured in a single image, preventing the reliable quantification of Foxo nuclear/cytoplasmic ratios. To measure nuclear Foxo fluorescence in the R2, TIFF images of the DAPI channel were opened with ImageJ and sections of the R2 closest to the R3 were manually outlined. The area outside of these regions of interest (ROIs) was cropped using the ''clear outside'' command and a threshold was manually applied to selectively outline nuclei. A mask was created and a watershed was applied to individualize the nuclei. Relevant nuclei were further filtered based on size (between 0.02 – infinity pixels) using the ''analyze particles'' command. This ''nuclear ROI'' was then applied to the TIFF image of the anti-Foxo stain to measure its mean pixel gray value. To measure cytoplasmic Foxo fluorescence, the ''nuclear ROI'' was cropped from the TIFF image of the anti-Foxo stain, the R2 ROI was reopened, and the area outside of this ROI was cropped. The image was then converted to 8-bit and a threshold was applied to selectively retain the cytoplasmic area and exclude the area previously occupied by nuclei. The command ''create selection'' was used to select and measure the mean pixel gray value in the cytoplasmic area. Foxo nuclear/cytoplasmic fluorescence ratio was then calculated for each image by dividing the nuclear mean pixel gray value by the cytoplasmic mean pixel gray value.

### Quantification of puc-lacZ fluorescence signal

Whole midgut TIFF images were opened with ImageJ and converted to 8-bit. Intestinal regions were manually outlined using the polygon selection tool. A threshold was applied to selectively outline positive nuclear staining (lacZ has a nuclear localization signal). The raw intensity of the thresholded area was measured in the different midgut regions. To account for differences in the size of the regions, the sum of the pixel values in the selection (raw integrated density) was divided by the area of the respective region.

### DNA extraction from tissues

10 intestines were dissected in PBS, transferred to homogenization microtubes containing 100 μL of sterile glass beads (1 mm diameter) and snap frozen in liquid nitrogen. Samples were stored at −80°C until DNA extraction. DNA was extracted using the Qiagen DNeasy Blood & Tissue Kit (Cat#69504). 180 μL of buffer ATL was added to the microtubes and tissues were homogenized using a Precellys 24 (Bertin technologies) at 5,000 rpm for 15 s. Subsequent steps for DNA extraction were performed according to the manufacturer's recommendations. DNA was used for qPCR analyses as described below.

### RNA extraction from tissues and cDNA synthesis

10 midguts, 20 midgut regions (R1-R5), or 10 dorsal abdomens were dissected in PBS, transferred to homogenization microtubes containing 100 μL of sterile glass beads (1 mm diameter) and snap frozen in liquid nitrogen. Samples were stored at −80°C until RNA extraction. Total RNA was extracted using the Promega Reliaprep RNA Tissue Miniprep System (Cat#Z6112). 500 μL of lysis buffer was added to the microtubes and tissues were homogenized using a Precellys 24 (Bertin technologies) at 5,000 rpm for 15 s. Subsequent steps for RNA extraction were performed according to the manufacturer's recommendations. Reverse transcription was performed on 0.25–1 μg RNA using Quantabio qScript cDNA Supermix (Cat#733–1178) following the manufacturer's recommendations. cDNA was used for qPCR analyses as described below.

### Quantitative PCR (qPCR)

Genomic or complementary DNA was used as template with Promega GoTaq qPCR Master Mix (Cat#A6001). qPCR reactions were performed according to the manufacturer's recommendations on an Applied Biosystem Quantstudio 3 instrument. Fold-of-change in genomic sequences or in transcript levels were determined using the ΔΔCt method. For the molecular characterization of the conditional *dHNF4* allele (Figure S2), the level of *dHNF4* genomic sequence ("$_g$*dHNF4*") was normalized to *Act5c* genomic sequence ("$_g$*Act5c*"). For RT-qPCR analyses, transcript levels were normalized to *rp49* (also known as *RpL32*). qPCR analyses were performed in four to five biological replicates. Independent experiments were repeated two to three times. One representative experiment is shown in the figures. A list of oligonucleotides used for qPCR analyses is provided in Table S4.

### mRNA-sequencing

20 intestines were dissected in PBS on ice and snap frozen in liquid nitrogen. Five biological replicates per genotype were generated and total RNA was extracted as described above. Library preparation and sequencing were performed by the Cologne Center for Genomics. Libraries were prepared using the Illumina Stranded Truseq RNA Sample Preparation Kit. ERCC RNA Spike-In Mix (ThermoFisher Scientific Cat#4456740) was added to the samples prior to library preparation. 1 μg of total RNA was used for library preparation. After poly-A selection (using poly-T oligo-attached magnetic beads), mRNA was purified and fragmented using divalent cations at elevated temperature. RNA fragments were reverse transcribed using random primers and second-strand cDNA synthesis was performed with DNA polymerase I and RNase H. After end repair and A-tailing, indexing adapters were ligated. The products were purified and amplified (15 PCR cycles) to generate the final cDNA libraries. After library validation and quantification (Agilent Tape Station), equimolar amounts were pooled. The pool was quantified by using the Peqlab KAPA Library Quantification Kit and

the Applied Biosystems 7900HT Sequence Detection System. The pool was sequenced on an Illumina NovaSeq6000 sequencing instrument using a PE100 protocol.

### Transcriptomic analysis

The quality of the sequencing reads was checked using FastQC. Sequencing reads were trimmed by using Trim Galore! software (https://www.bioinformatics.babraham.ac.uk/projects/trim_galore/) and the following adapters:

Read1:
AGATCGGAAGAGCACACGTCTGAACTCCAGTCA.
- AGATCGGAAGAGCACACGTCTGAAC.
- TGGAATTCTCGGGTGCCAAGG.
- AGATCGGAAGAGCACACGTCT.
- CTGTCTCTTATACACATCT.
- AGATGTGTATAAGAGACAG.

Read2:
- AGATCGGAAGAGCGTCGTGTAGGGAAAGAGTGT.
- AGATCGGAAGAGCGTCGTGTAGGGA.
- TGGAATTCTCGGGTGCCAAGG.
- AGATCGGAAGAGCACACGTCT.
- CTGTCTCTTATACACATCT.
- AGATGTGTATAAGAGACAG.

*D. melanogaster* annotated transcripts (BDGP6.32) were downloaded from Ensembl. Transcript abundance was estimated by using Kallisto-quant (https://pachterlab.github.io/kallisto/manual, ver. 0.64.0.). Read count normalization was performed by adjusting to ERCC spike-in controls and differential gene expression analysis was performed by RUVSeq and edgeR Bioconductor R packages. GO term enrichment analysis was performed with Metascape.[68]

### Transmission electron microscopy

Sections of the intestine were dissected in PBS and fixed with 2% Formaldehyde (Science Services, E15700) and 2% Glutaraldehyde (Merck, 354400) in 0.1 M Cacodylate buffer for 48 h. For convenient transfer of liquids, tissues were placed in Corning Netwells (Merck, CLS3479-48EA) and postfixed with 1% osmium tetroxide (Science Services, E19140) and 1% potassium hexacyanoferrate (Merck, 13746-66-2) for 1 h at 4°C. After three 5-min washes with double distilled water, the samples were dehydrated using an ascending ethanol series (50%, 70%, 90%, 100%) for 10 min each. Infiltration was performed with a mixture of 50% Epon/ethanol for 2 h, 70% Epon/ethanol for 2 h and overnight with pure Epon (Merck, 45345). After 2 h of fresh Epon, the tissues were mounted into flat embedding molds and cured at 60°C for 48 h. Samples were trimmed to the region of interest using razor blades. Ultrathin sections (70 nm) were cut with a diamond knife (Science Service, DH4540) on a UC6 ultramicrotome (Leica) and collected on pioloform coated slot grids. Poststaining was performed with 1.5% uranyl acetate (Agar Scientific, Stansted, United Kingdom) for 15 min and Reynolds lead citrate solution (Roth, Karlsruhe, Germany) for 3 min. Images were acquired using a JEM-2100 Plus transmission electron microscope (JEOL) operating at 80 kV and equipped with a OneView 4K camera (Gatan).

### Sample preparation for lipidomic analyses

20 flies, 40 intestines or 30 dorsal abdominal cuticles containing adipose tissue were collected for the analysis of triacylglycerol and fatty acids. Samples were homogenized in Milli-Q water (20 flies in 300 μL, 40 intestines or 30 dorsal cuticles in 200 μL) using a Precellys 24 device (Bertin technologies) at 6,500 rpm for 30 s. The protein content of the homogenate was determined using bicinchoninic acid.

### Hemolymph collection

The thorax was punctured with a 0.8 × 38 mm needle under anesthesia. 50 punctured flies were then placed in the center of a 47 mm, 20 μm pore size nylon membrane filter (Sigma Aldrich NY2004700). The nylon membrane was then folded to trap the flies, and transferred to a 1.5 mL safe-lock microcentrifuge tube. The nylon membrane was held in the upper half of the tube by trapping its corners under the safe-lock lid. This avoids contact with the bottom of the tube, where hemolymph is collected after centrifugation at 3500 rcf for 3 min at 4°C. The hemolymph samples were then placed on dry ice prior to long-term storage at −80°C.

### Analysis of triacylglycerols by lipidomics

450 μL of Milli-Q water, 1.875 mL of chloroform/methanol/37% hydrochloric acid (5:10:0.15, volume/volume) and 30 μL of d5-TG internal standard mixture I (Avanti Polar Lipids) were added to whole-fly or tissue homogenates (50 μL). Lipid extraction was performed as previously described.[69] Triacylglycerols were analyzed by Nano-Electrospray Ionization Tandem Mass Spectrometry (Nano-ESI-MS/MS) with direct infusion of the lipid extract (*Shotgun Lipidomics*) as previously described.[70,71] Endogenous lipid species were quantified by referring their peak areas to those of the respective internal standard. The calculated lipid amounts were normalized to the protein content of the homogenate. Three independent experiments were performed to score triacylglycerol

contents in whole flies. Two independent experiments were performed to score triacylglycerol contents in dorsal abdominal cuticles. We scored midgut triacylglycerol contents once.

### Analysis of hemolymph DAG by lipidomics

Diacylglycerols (DAG) were extracted from hemolymph using previously described methods,[72] with modifications. 200 μL of 155 mM ammonium carbonate buffer, 990 μL of chloroform/methanol 17:1 (v/v) and 10 μL each of 4 μM d5-DG Internal Standard Mixtures I and II (Avanti Polar Lipids) were added to 1 μL of hemolymph. Lipids were extracted by shaking at 900 rpm/min in a ThermoMixer (Eppendorf) at 20°C for 30 min. After centrifugation (12,000xg, 10 min, 4°C), the lower (organic) phase was transferred to a new tube, and the upper phase was extracted again with 990 mL chloroform/methanol 2:1 (v/v). The combined organic phases were dried under a stream of nitrogen. The residue was resolved in 100 μL methanol. Diacylglycerols were analyzed by Nano-Electrospray Ionization Tandem Mass Spectrometry (Nano-ESI-MS/MS) with direct infusion of the lipid extract (Shotgun Lipidomics) as previously described.[70,71] Endogenous lipid species were quantified by referring their peak areas to those of the respective internal standard. The calculated lipid amounts were normalized to the volume of hemolymph. Diacylglycerols were scored once in the hemolymph of $tub^{ts}>Nplp2_i^{VDRC}$ and $mex>dHNF4_i^{TRiP}$ animals and their respective controls.

### Fatty acid profiling

500 μL of methanol, 250 μL of chloroform and internal standard (0.5 μg palmitic-d31 acid) were added to intestinal homogenates (100 μL). The mixture was sonicated for 5 min, and lipids were extracted in a shaking bath at 48°C overnight. Glycerolipids were degraded by alkaline hydrolysis by adding 75 μL of 1 M potassium hydroxide in methanol. After sonication for 5 min, the extract was incubated for 2 h at 37°C and neutralized with 6 μL of glacial acetic acid. 2 mL of chloroform and 4 mL of water were added to the extract, which was vortexed vigorously for 30 s and centrifuged (4,000 x g, 5 min, 4°C) to separate the layers. The lower (organic) phase was transferred to a new tube, and the upper phase was extracted with 2 mL of chloroform. The combined organic phases were dried under a nitrogen stream. Residues were resolved in 200 μL of acetonitrile/water (2:1, volume/volume) and sonicated for 5 min. After centrifugation (12,000 x g, 10 min, 4°C), 40 μL of the supernatants were transferred to autoinjector vials.

Fatty acid levels were determined by LC-ESI-MS/MS using a previously described method with minor modifications.[73] 10 μL of sample was loaded onto a Core-Shell Kinetex Biphenyl column (100 mm × 3.0 mm ID, 2.6 μm particle size, 100Å pore size, Phenomenex), and fatty acids were detected using a QTRAP 6500 triple quadrupole/linear ion trap mass spectrometer (SCIEX). The LC (Nexera X2 UHPLC System, Shimadzu) was operated at 40°C and at a flow rate of 0.7 mL/min with a mobile phase of 5 mM ammonium acetate and 0.012% acetic acid in water (solvent A) and acetonitrile/isopropanol 80:20 (v/v) (solvent B). Fatty acids were eluted with the following gradient: initial, 55% B; 4 min, 95% B; 7 min, 95% B; 7.1 min, 55% B; 10 min, 55% B.

Fatty acids were monitored in negative ion mode using "pseudo" Multiple Reaction Monitoring (MRM) transitions.[73] The instrument settings for nebulizer gas (Gas 1), turbogas (Gas 2), curtain gas, and collision gas were 60 psi, 90 psi, 40 psi, and medium, respectively. The interface heater was on, the Turbo V ESI source temperature was 650°C, and the ionspray voltage was −4 kV.

The LC chromatogram peaks of the endogenous fatty acids and the internal standard palmitic-d31 acid were integrated using the MultiQuant 3.0.2 software (SCIEX). Endogenous fatty acids were quantified by normalizing their peak areas to those of the internal standard. The normalized peak areas were then normalized to the protein content of the homogenate. Intestinal fatty acid content was analyzed once.

### Enzymatic quantification of total TAG levels

Triacylglycerol (TAG) levels were determined in thoraces using Sigma free glycerol and triglyceride reagents (F6428-40ML and T2449-10ML, respectively), as previously described.[15] 15 thoraces were homogenized in 120 μL PBS for enzymatic quantification of TAGs. TAG levels were normalized to protein contents in tissue homogenates. For protein quantification, 10 μL of tissue homogenates were diluted in 190 μL PBS and 10 μL of this solution was mixed with 200 μL of Bio-Rad Protein Assay Dye (Cat#5000006, diluted 1:4 in MilliQ water (v/v)) and incubated for 5 min at room temperature. Absorbance was then read at 595 nm. Protein concentration in homogenates was determined using a standard curve generated with diluted BSA samples. TAG levels were determined in five biological replicates per genotype. Three independent experiments were performed.

### Determination of intestinal lipase activity

Intestinal lipase activity was determined using Sigma Aldrich Lipase Activity Assay Kit (MAK047) and a Multiscan SkyHigh microplate spectrophotometer (Thermofisher scientific). 30 intestines were dissected in PBS on ice, transferred to safe-lock reaction tubes and snap frozen in liquid nitrogen. Samples were stored at −80°C until determination of lipase activity. Tissues were rapidly homogenized in 90 μL assay buffer using a motor and pestle and the homogenates were centrifuged at 13,000 x g for 10 min at 4°C to precipitate insoluble material. 50 μL of supernatant was transferred to a 96-well plate and subsequent steps were performed according to manufacturer's recommendations. Lipase activity was normalized to the protein content of the samples. Protein quantification was performed as described above. Intestinal lipase activity was determined in five biological replicates per genotype. Three independent experiments were performed.

### Analysis of cuticular hydrocarbons (CHCs)

Extractions of individual flies were performed in 2 mL glass vials (Agilent Technologies, Santa Clara, California, USA) on an orbital shaker for 10 min. Extracts were subsequently evaporated under a constant stream of gaseous carbon dioxide and then resuspended in 5 μL of a hexane solution containing 7.5 ng/μL dodecane (C12) as an internal standard. Following this, 3 μL of the resuspended extracts were injected in splitless mode with an automatic liquid sampler (ALS) (PAL RSI 120, CTC Analytics AG, Switzerland) into a gas-chromatograph (GC: 7890B) simultaneously coupled to a flame ionization detector (FID: G3440B) and a tandem mass spectrometer (MS/MS: 7010B, all provided by Agilent Technologies, Waldbronn, Germany). The system was equipped with a fused silica column (DB-5MS ultra inert; 30 m × 250 μm x 0.25 μm; Agilent J&W GC columns, Santa Clara, CA, USA) at a temperature of 300°C with helium used as a carrier gas under a constant flow of 1.8 mL/min. The FID had a temperature of 300°C and used nitrogen with a 20 mL/min flow rate as make-up gas and hydrogen with a 30 mL/min flow rate as fuel gas. The column was split at an auxiliary electronic pressure control (Aux EPC) module into an additional deactivated fused silica column piece (0.9 m × 250 μm) with a flow rate of 0.8 mL/min leading into the FID detector, and another deactivated fused silica column piece (1.33 m × 250 μm) at a flow rate of 1.33 mL/min into the mass spectrometer. The column temperature program started at 60°C and was held for 5 min, increasing 20°C/min up to 200°C where it was held for 5 min again, and then increasing 3°C/min to the final temperature of 325°C, with another holding time of 5 min.

CHC peak detection, integration, quantification and identification were all carried out with Quantitative Analysis MassHunter Workstation Software (Version B.09.00/Build 9.0.647.0, Agilent Technologies, Santa Clara, California, USA). CHCs were identified according to their retention indices, diagnostic ions, and mass spectra as provided by the total ion count (TIC) chromatograms, whereas their quantifications were achieved by the simultaneously obtained FID chromatograms, allowing for the combination of the best-suited method for hydrocarbon quantification (Agilent Technologies, Waldbronn, Germany, pers. comm.) with reliable compound identifications. Absolute CHC quantities (in ng) were obtained by calibrating each compound based on the closest eluting *n*-alkane obtained from from a C21-40 standard dilution series (Merck, KGaA, Darmstadt, Germany) with concentrations of 0.5, 1, 2, 5, 10, 20, and 40 ng/μL, respectively, run in three replicates (except for 5 ng/μL concentration, where only two replicates could be used) for calibration curve calculation.

### Information related to the experimental design

Blinding was not used in the course of our study. No data or subjects were excluded from our analyses, unless otherwise stated in the methods.

## QUANTIFICATION AND STATISTICAL ANALYSIS

Graphical representation and statistical analysis of the data were performed using GraphPad Prism 8 software (www.graphpad.com), except for the representation of cuticular hydrocarbon variation.

For transcript analysis by RT-qPCR, the data are presented as box and whiskers plots. The box extends from the 25th to the 75th percentile, the line represents the median, and the whiskers represent the minimum and maximum values. Dots represent biological replicates (samples of 10 midguts, 20 midgut regions (R1-R5), or 10 dorsal abdomens). Transcript levels are presented as relative to control values. Two to three independent experiments were performed, one representative experiment is shown. Mann-Whitney test was used for pairwise comparisons. Asterisks indicate statistically significant differences between conditions. $0.001<^{**}p < 0.01$; $0.01<^{*}p < 0.05$. ns = no statistically significant difference with controls.

For transcript analysis by mRNA-seq, average log2 fold changes in transcript levels are presented as heat maps. Log2 fold changes were calculated from five biological replicates for each genotype. Only transcripts with significant differences in their levels are shown on the heat maps. The statistical significance of non-redundant gene ontology terms (Biological Processes) enriched in the list of up- or down-regulated transcripts is presented as a bar graph with a discrete color scale.

For the quantification of pHH3 positive cells per midgut, the data are presented as individual values. Each dot represents the number of pHH3-positive cells in a single midgut, the horizontal line represents the median. Pooled values from three independent experiments are shown. $n = 17$ and 27 midguts for controls and *mex>dHNF4 RNAi*, respectively. Mann-Whitney test was used for pairwise comparisons. Asterisks illustrate statistically significant differences between conditions. $^{****}p < 0.0001$.

For lifespan studies, data are presented as Kaplan-Meier survival plots. The number of animals used in the lifespan experiments and the median lifespan in each condition are indicated in the figure legends. A log rank (Mantel-Cox) test was used for statistical comparison of survival plots. The *p*-value is indicated in the figure legends when the difference is statistically significant.

For the analysis of food intake, the number of sips on standard food is presented as individual values. Dots represent single animals. Pooled values from three independent experiments are shown. Mann-Whitney test was used for pairwise comparisons. ns = no statistically significant difference between conditions.

For the analysis of fatty acids by lipidomics, the data are presented as box and whiskers plots. The box extends from the 25th to the 75th percentile, the line represents the median, and the whiskers represent the minimum and maximum values. Dots represent biological replicates (samples of 40 midguts). Fatty acid levels are presented as relative to control values. Fatty acid profiling was performed once. Mann-Whitney test was used for pairwise comparisons. Asterisks indicate statistically significant differences from controls. $0.001<^{**}p < 0.01$; $0.01<^{*}p < 0.05$.

For the analysis of tri- and diacylglycerol levels by lipidomics and with enzymatic assays, the data are presented as box and whiskers plots. The box extends from the 25th to the 75th percentile, the line represents the median, and the whiskers represent the minimum and maximum values. Each dot represents a biological replicate (sample containing hemolymph from pooled individuals, several flies or tissues, please refer to the methods for more information). Pooled values from one to three independent experiments are shown. Mann-Whitney test was used for pairwise comparisons. Asterisks indicate statistically significant differences between conditions. $0.001 < {}^{**}p < 0.01$; $0.01 < {}^{*}p < 0.05$.

For the determination of intestinal lipase activity, the data are presented as individual values. Each dot represents a biological replicate (sample of 30 midguts), the horizontal line represents the median. Pooled values from three independent experiments are shown, $n = 15$ for controls and *mex>dHNF4 RNAi*. Mann-Whitney test was used for pairwise comparisons. Asterisks indicate statistically significant differences between conditions. ${}^{****}p < 0.0001$.

For the quantitative analysis of Oil Red O stains, the data are presented as individual values. Dots represent single midgut regions; the horizontal line represents the median. Pooled values from two to four independent experiments are shown. Mann-Whitney test was used for pairwise comparisons. Asterisks indicate statistically significant differences between conditions. ${}^{****}p < 0.0001$; $0.0001 < {}^{***}p < 0.001$; $0.001 < {}^{**}p < 0.01$; $0.01 < {}^{*}p < 0.05$. ns = no statistically significant difference between conditions.

For the graphical representation of high-dimensional cuticular hydrocarbon variation into two dimensions, the ordination method "nonmetric multidimensional scaling" (NMDS) from the R package "vegan" was used (https://cran.r-project.org/web/packages/vegan/index.html).[74] Reducing the dimensionality with this method, the data points are plotted in a monotonous way so that the calculated distances ($\delta$) in the plot give the most accurate reflection of the actual distances (d) between the data. Two preconditions are met with the NMDS method.

(1) The calculated distances in the plot are smaller or equal to the actual data point distances ($\delta_{i,j} \leq d_{i,j}$)
(2) The correlation between the calculated distances and the actual data point distances is maximized ($\mathrm{cor}(\delta_{i,j}, d_{i,j}) \leftrightarrow \max$)

To access the quality of the NMDS, stress values have been calculated and are indicated in the figure legends.[43] Each dot on the plot represents a specimen of the indicated genotype. The analysis of cuticular hydrocarbon was performed once.

For the quantitative analysis of puc-lacZ fluorescence signal, the data are presented as box and whiskers plots. The box extends from the 25th to the 75th percentile, the line represents the median, and the whiskers represent the minimum and maximum values. Dots represent biological replicates (single midgut regions). Pooled values from three to four independent experiments are shown. Mann-Whitney test was used for pairwise comparisons. Asterisks indicate statistically significant differences from controls. ${}^{****}p < 0.0001$; $0.0001 < {}^{***}p < 0.001$; $0.001 < {}^{**}p < 0.01$; $0.01 < {}^{*}p < 0.05$. ns = no statistically significant difference between conditions.

For the quantification of Foxo nuclear/cytoplasmic fluorescence ratio, the data are presented as box and whiskers plots. The box extends from the 25th to the 75th percentile, the line represents the median, and the whiskers represent the minimum and maximum values. Dots represent biological replicates (single midguts). Pooled values from four independent experiments are shown. Mann-Whitney test was used for pairwise comparisons. Asterisks indicate statistically significant differences from controls. $0.01 < {}^{*}p < 0.05$.

Details regarding statistical analysis can also be found in the figure legends.